

INFRARED SPECTROSCOPIC STUDIES OF MATRIX-ISOLATED
MOLECULES WITH POTENTIAL ASTROPHYSICAL SIGNIFICANCE

By
CHRISTINE MARIE WEHLBURG

A DISSERTATION PRESENTED TO THE GRADUATE SCHOOL
OF THE UNIVERSITY OF FLORIDA IN PARTIAL FULFILLMENT
OF THE REQUIREMENTS FOR THE DEGREE OF
DOCTOR OF PHILOSOPHY

UNIVERSITY OF FLORIDA

1997

To the ones I love...

ACKNOWLEDGMENTS

Sincere thanks to Dr. Jan Szczepanski for all his guidance, support and exasperating attention to detail. I would like to thank Dr. Martin Vala for his *gentle* nudging and undaunted approach to editing a dissertation written by a quintessential procrastinator. Since financial support is never a trivial detail, a grateful acknowledgment to the National Aeronautics and Space Administration for supporting these research projects and contributing to my fellowship for three years.

My husband, Joe, is my inspiration. What I am today, is unequivocally due to the fact that he loves me. I would like to thank my father for giving me the joy of learning and my mother for giving me strength. Special thanks also to my extended family, Dr. and Mrs. A. F. C. Wehlburg, for their encouragement and advice.

TABLE OF CONTENTS

ACKNOWLEDGMENTS.....	iii
ABSTRACT.....	vi
CHAPTERS	
I. INTRODUCTION	1
II. INFRARED INVESTIGATIONS OF PAH IONS	4
A. Background	4
1. The Unidentified Infrared (UIR) Emission and PAHs.....	4
2. Previous Work	14
B. Experimental	17
C. Pentacene Cations and Anions	22
1. Electronic Spectra	22
2. Infrared Spectra.....	27
3. Vibrational Analysis	36
D. Tetracene Cations and Anions	40
1. Electronic Spectra	40
2. Infrared Spectra.....	44
3. Integrated Intensities of Infrared Transitions.....	50
4. Vibrational Analysis	53
E. Discussion	57
1. Ionization Mechanisms	57
2. Fragmentation of PAHs	59
3. Photolysis Process.....	60
4. PAH Intensities and their Correlation with UIR Emission.....	62
5. PAH Ions in Interstellar Space.....	64
III. INFRARED INVESTIGATIONS OF CARBON CLUSTERS.....	73
A. Carbon Clusters and their Astrophysical Connection.....	73
B. Experimental	77
C. $C_n \cdot H_2O$ Complexes	80
1. Infrared Spectra.....	80
2. Theoretical Results.....	86
3. Isotopomer Assignments for $C_6 \cdot H_2O$	90
D. C_3^- Molecule	99
1. Infrared Absorption Spectra.....	99

2. Theoretical	102
3. Discussion	110
IV. CONCLUSIONS	112
A. PAHs	112
B. $C_n \cdot H_2O$ Complexes	113
C. C_3^- Molecule.....	114
REFERENCES.....	115
BIOGRAPHICAL SKETCH.....	121

Abstract of Dissertation Presented to the Graduate School
of the University of Florida in Partial Fulfillment of the
Requirements for the Degree of Doctor of Philosophy

INFRARED SPECTROSCOPIC STUDIES OF MATRIX-ISOLATED
MOLECULES WITH POTENTIAL ASTROPHYSICAL SIGNIFICANCE

By

Christine Marie Wehlburg

August 1997

Chairperson: Martin T. Vala
Major Department: Chemistry

Many of the molecules purported to exist in interstellar space can only be generated in high temperature processes or are ions that are difficult to produce at high enough concentrations for spectroscopic analysis. The molecules investigated in this study, specifically, were polycyclic aromatic hydrocarbon (PAH) ions, carbon chain water complexes and carbon chain anions.

PAHs are the proposed carriers of the unidentified interstellar (UIR) emission. The infrared investigation of pentacene and tetracene ions was pursued to provide data concerning the possibility that PAH cations were the source of the UIR emission. In this study, infrared features corresponding to both cation and anions for both molecules were observed for the first time. The most intense features for the neutral molecules were the CH out-of-plane wagging modes while the most intense cationic and anionic features were in the CC stretch and CH bending regions. The relative intensities from theoretical calculations were in reasonable agreement with experimental values with the exception of an overestimation for the intensities of the CH stretch in both neutral pentacene and tetracene.

Carbon chain water complexes are very weakly bound species that are observed when graphite is vaporized at low power. The infrared features increase in intensity and new ones appear after annealing a matrix containing carbon chain molecules and H_2O . The current study involved assignment of infrared features at 1959.4 and 2014.4 cm^{-1} to $\text{C}_6\bullet\text{H}_2\text{O}$ and $\text{C}_9\bullet\text{H}_2\text{O}$, respectively. Assignments were based on the fact that both bands increased relative to the C_9 and C_6 bands when the concentration of H_2O increased. The band assignments were further justified by a $^{12,13}\text{C}$ study for $\text{C}_6\bullet\text{H}_2\text{O}$ and the agreement of the theoretical shift, relative to the asymmetric stretch band of C_9 , for $\text{C}_9\bullet\text{H}_2\text{O}$. In addition a new feature at 1550.4 cm^{-1} was tentatively assigned to $\text{C}_4\bullet\text{H}_2\text{O}$.

Finally, an isotopic study of a feature at 1721.8 cm^{-1} confirmed the assignment of the band to the asymmetric stretching mode of linear C_3^- . The calculated isotopic shifts are in very good agreement. In addition, calculations based on the GF matrix method confirmed a linear structure for C_3^- in an Ar matrix.

I. INTRODUCTION

Matrix isolation involves mixing vapor phase species with a high concentration of inert gas and condensing the mixture on a cold surface that is sufficiently low temperature to solidify the isolant gas. Phosphorescence studies by Lewis and Lipkin in the 1940's had trapped aromatic molecules in cold glassy matrices¹. Norman and Porter² and Pimentel's group³ introduced the technique of trapping molecules in inert matrices in 1954. Matrix isolation was proposed for the experimental investigations of unstable constituents. Transient species can be trapped and isolated in the solid matrix thereby preventing reactions or rapid decomposition that would occur in gas phase studies. Species that are produced in the gas phase at concentrations below the limit of detection can be deposited over time and a quantity of molecules sufficiently large enough to interrogate can be "built-up". Additional species can also be generated by post-deposition processes that include photolysis and warming the matrix (annealing)⁴.

Spectroscopy of matrix-isolated species has found a niche in the study of molecules implicated in astrophysical objects and believed to be responsible for spectral features gathered from various celestial objects. Many of the molecules purported to exist in interstellar space are radicals or ions, or they can only be generated in high temperature processes. These transient or highly reactive species are especially suited to matrix-isolation investigations. In addition, the environmental conditions of matrix-isolation are believed to mimic the frigid temperatures and "isolation" of species associated with interstellar space. At first glance, matrix isolation sounds like the perfect

medium of choice for spectroscopic studies. However there are some limitations that need to be considered.

The species of interest in matrix-isolation studies are isolated from each other but they are not exactly in a non-interacting, low pressure gas-phase environment. The chosen isolant gas must be non-reactive and, in the case of optical spectroscopy, transparent in the wavelength region of interest. Perturbation effects by the isolant material on the species once the two have condensed on the cold surface must also be considered. Interactions with the matrix host can lead to frequency shifts compared to gas-phase results and the occupation of different "sites" in the matrix, can cause band broadening, splitting or changes in spectral shape. Isolant gases commonly chosen for matrix-isolation spectroscopic studies are the noble gases because they are essentially inert, optically transparent and, since they have low polarizabilities, perturb the molecule the least.

At the cryogenic temperatures associated with inert gas matrices (Ne~4 K; Ar~10 K), the isolated species are usually trapped in their ground electronic and vibrational states. The features observed in infrared investigations of these molecules correspond to transitions from the ground state only and will be very sharp due to the elimination of "hot bands" associated with transitions from vibrational levels normally occupied at higher temperatures. While the sharpness of the bands makes identification of the IR active fundamentals very direct, there is essentially little rotational data available in matrix-isolation studies. Therefore, information normally ascertained from the rotational structure in spectroscopic gas phase investigations is not available using matrix isolation

techniques . Gas phase studies, however, require a constant generation of the species of interest at concentrations above the limit of detection.

The elimination of hot bands in the spectrum of a matrix-isolated species is an advantage when performing isotopic studies. In the analysis of carbon vapor, the ubiquity of possible constituents has necessitated isotopic studies to positively identify spectral features. Another advantage in matrix isolation is the ability to anneal the matrix to temperatures below the sublimation temperature of the isolant gas. Annealing allows the isolated species to diffuse in the "softened" matrix. In the study of carbon vapor, annealing not only permits the formation of larger carbon clusters but also the formation of water clusters whose transient nature would not permit observation under room temperature conditions. The generation of these species upon annealing of the matrix is proposed to simulate possible reaction pathways on interstellar grains.

Because of the photon flux in the interstellar medium, ions play an important role in interstellar chemistry. The laboratory production of gas phase ions from neutral molecules, however, is not always a very efficient process. By depositing an ion/neutral mixture in a matrix isolation experiment over a long period of time, the number of ions can be built up to an amount sufficient for spectroscopic analysis. In addition, the deposited species can also be subjected to additional processes such as photolysis in order to produce new species or correlate the behavior of specific features.

II. INFRARED INVESTIGATIONS OF PAH IONS

A. Background

1. The Unidentified Infrared (UIR) Emission and PAHs

One of the most perplexing problems in astrophysics has been the origin of the infrared emission features first discovered by Gillet, Forrest and Merrill in 1973⁵. These features, now known to be associated with many celestial objects, exhibit sharp features at 3.3, 6.2, 7.7, 8.7 and 11.3 μm (3040, 1615, 1300, 1150 and 885 cm^{-1} , respectively). Other minor and broad features have also been located at 3200-2700 cm^{-1} (3.1-3.7 μm), 1660-1100 cm^{-1} (6.0-9.0 μm) and 910-770 cm^{-1} (11.0-13.0 μm)⁶. Figure 1 depicts the UIR emission spectra from three representative sources: (A) An HII/starforming region of the Orion⁷ (B) Central region of the galaxy M82.⁸ and (C) Planetary nebula NGC 2023⁹.

Based on the ratio of intensities of the 3.3 μm band to the remaining lower frequency features, Allamandola and Norman proposed in 1978 that the source of the emissions was small molecules frozen (10 K) in dust grains emitting infrared fluorescence (IRF) after being UV pumped¹⁰. In 1981, Duley and Williams proposed that the bands were produced by functional groups attached to aromatic constituents on thermally excited dust grains¹¹. The aromatics were a mixture of randomly oriented clusters and sheets identified as hydrogenated amorphous carbon (HAC) particles. These

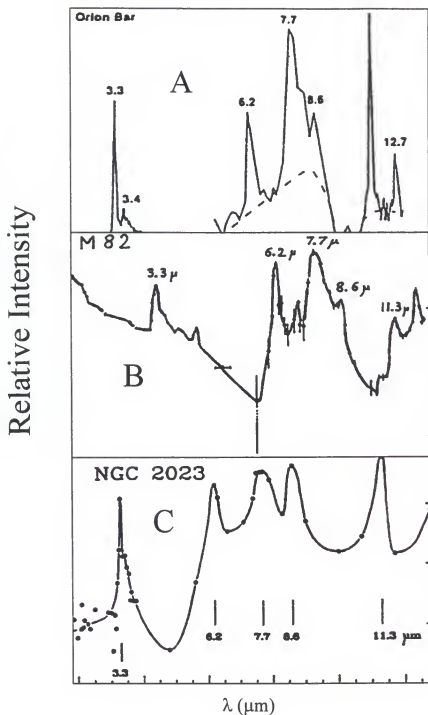


Figure 1. UIR emission spectra from three sources. (A) An HII/starforming region of the Orion bar adapted from Schutte *et al*⁷. (B) Central region of the galaxy M82 adapted from Willner *et al*⁸. (C) Planetary nebula NGC 2023 adapted from Russel *et al*⁹.

early ideas laid the foundation for the current hypothesis that IRF emitted from UV-pumped molecular PAHs are responsible for the UIR emission.

The UIR emission from different sources show variations in the ratios of band intensities. Consequently, it was proposed that they originated not from any single molecule but from a family of related molecules¹². In addition, the fractional intensity of the $\sim 1300\text{ cm}^{-1}$ feature has been determined to be related to the amount of carbon believed to be available in the specific UIR source (i.e. planetary nebulae, reflection nebulae, HII regions and galaxies)¹³. Most of the analyses of the UIR emission have concentrated on the strong features at 3.3, 6.2, 7.7, 8.7 and 11.3 μm . The sharpness of these bands was the initial indicator pointing toward a molecular source for the UIR. The broad features in the regions 6.0-9.0 μm and 11.0-13.0 μm have been proposed to originate from very large PAHs, PAH clusters and/or HAC⁶. The proposed relationship between PAHs and HAC is depicted in Figure 2.

In 1984, Léger and Puget proposed that partially dehydrogenated molecular PAHs could be the source of the UIR emission features¹⁴. In their investigation of small grains containing up to 50 carbon atoms as the source of the emission, they concluded that large planar polycyclic aromatic hydrocarbons could better explain the emission than small graphitic spheres. Figure 3B is a schematic of the energy levels for a neutral PAH to aid in the discussion of the infrared emission process. Léger and Puget proposed that upon absorption of UV radiation, a PAH molecule is excited to an excited singlet state. The excited state molecule undergoes internal conversion to the vibrationally excited S_0 state and then relaxes via infrared emissions. Based on room temperature absorption spectra ($T=300\text{ K}$), the emission spectra for several PAHs were calculated and are presented in

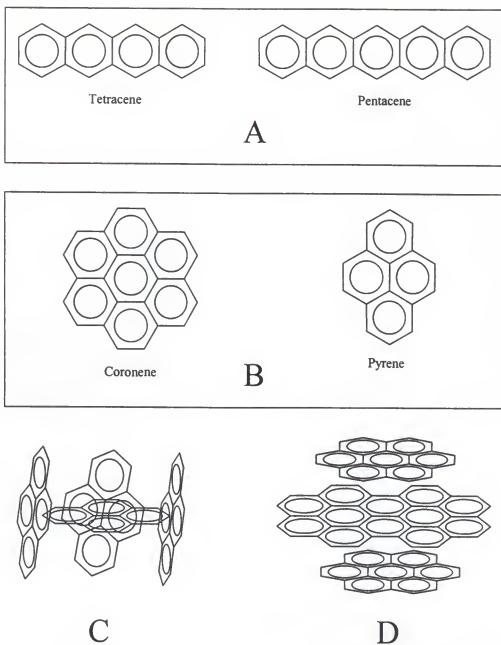


Figure 2. Various forms of polycyclic aromatic hydrocarbons (PAHs) proposed to exist in interstellar matter. (A) Catacondensed PAHs. (B) Pericondensed PAHs. (C) PAH clusters. (D) PAH sheets.

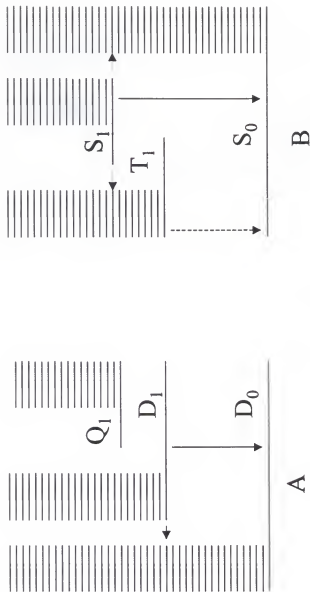


Figure 3. Energy level diagrams for polycyclic aromatic hydrocarbons (PAHs). (A) PAH cation. (B) PAH neutral. Adapted from Leach¹⁸.

Figure 4. The correlation of the calculated emission with the UIR emission (reflection nebula NGC 2023) was very promising for the PAH hypothesis¹⁵.

Independently of the proposal that molecular PAHs were the source of the UIR emissions, Allamandola *et al* proposed that partially hydrogenated PAH *cations* were responsible¹⁶. Since laboratory data for the ions did not exist, models used to support this proposal were based on fully hydrogenated neutral molecules. Using neutral chrysene as an example, Allamandola *et al* calculated theoretical IR emissions based on the strong $S_2 \leftarrow S_0$ absorption (See Figure 3B for energy level diagram of neutrals) near 267.5 nm¹⁷ ($37,400\text{ cm}^{-1}$). Intersystem crossing to the lowest triplet state of chrysene at about 20,000 cm^{-1} above the ground state left the remaining 17,400 cm^{-1} of excitation to be distributed over the vibrational modes of the T_1 triplet state. Infrared fluorescence emission of the neutral chrysene molecule was proposed to occur from the triplet state. It was noted that in the case of a PAH cation, the electronic states are doublets and quartets. The energy level diagram for cationic PAHs is presented Figure 3A. Since the first excited doublet state of PAH cations lies lower in energy than the first quartet state¹⁸, intersystem crossing to the quartet state (analogous to the crossing from the excited singlet state to the triplet state in neutral PAHs) would not occur. Vibrational emission would occur in the ground doublet state.

The primary difference between the two molecular PAH proposals was the vibrational population assumption. Léger *et al* based their calculated emission spectra on a thermal population distribution. According to their calculations, there was enough time to redistribute the energy among the vibrational levels due to the delay in time ($\tau \sim 10^{-1}\text{ sec}$) before the first IR photon was emitted¹⁵. Figure 5 illustrates the effect of

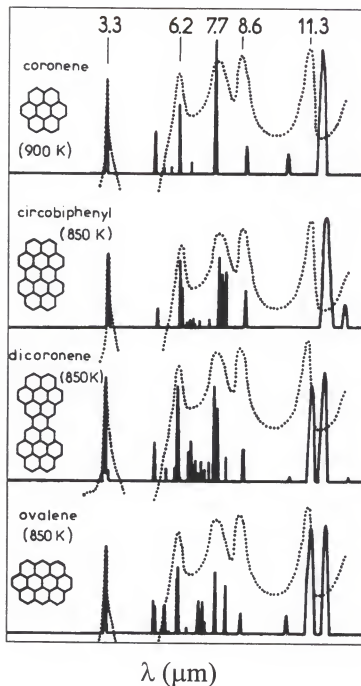


Figure 4. Emission spectra of several PAHs calculated from room temperature absorption spectra. The dotted line represents UIR emissions from the reflection nebula NGC 2023 for comparison. Adapted from Léger and d'Hendecourt¹⁵.

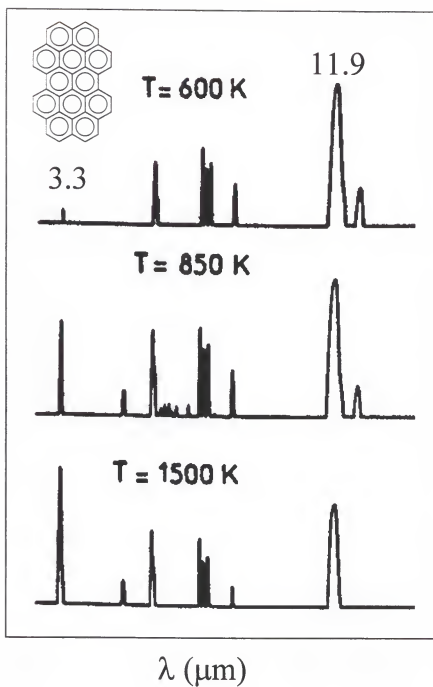


Figure 5. Calculated emission spectrum, based on the absorption spectrum, of circobiphenyl at different temperatures. Adapted from Leger and d'Hendecourt¹⁵.

temperature on the calculated emission spectrum of a PAH using a thermal population distribution. At higher temperatures, the calculated emission for PAH neutrals begin to resemble the UIR emission. Alternatively, the criteria for the theoretical emission calculated by Allamandola *et al* was a nonthermal population distribution¹⁶. Figure 6 shows the emission spectra of chrysene calculated as a function of vibrational energy content. The relative intensities of the fluorescence spectrum at excitation above 20,000 cm^{-1} also begins to resemble the UIR emission.

Regardless of the vibrational population approximation used, both methodologies attempted to explain the intensity differences between neutral PAHs and the UIR emission. However, there is still the issue of the UV rich environment of many interstellar objects. Absorption of a UV photon is expected to produce a stable ion, induce the loss of an H atom or photoisomerize the molecule to a more stable¹⁹, pericondensed, form²⁰. (Figure 2 shows examples of both catacondensed and pericondensed PAHs where the differentiating features are the fused rings and lack of non-adjacent hydrogen atoms in pericondensed molecules.) Infrared absorption data had been collected for neutral molecules, but there were no infrared data available for the cationic molecules. With first ionization potentials below 13.6 eV¹⁸, PAH cations had a proposed relative abundance estimated at 50% and higher compared to the neutral molecules^{21,22}. The matrix isolation FT-IR spectroscopic studies on pentacene and tetracene ions reported in this dissertation form an important part of the data needed to test the proposal that PAHs are the source of the UIR emission.

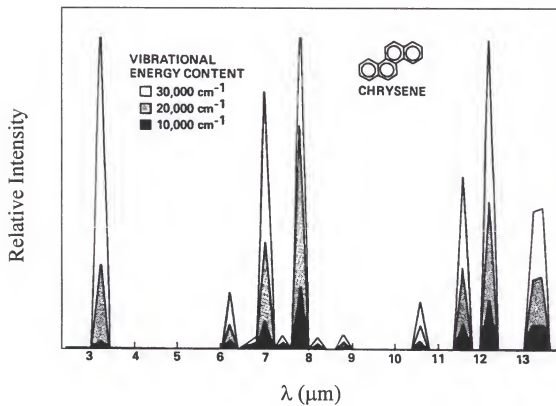


Figure 6. Emission spectra of chrysene calculated as a function of vibrational energy content. Adapted from Allamandola *et al*¹⁶.

2. Previous Work

Ions were produced in this study by passing a mixture of matrix isolant gas and PAH neutral through an electron beam. Previous studies on the PAH, anthracene, using the same ionization mechanism, calculated an $\sim 10\%$ ratio²³ of cation production versus the neutral molecule being deposited. Therefore, identification of the neutral PAH infrared features was the first step in identifying new infrared features that could be assigned to an ion. Infrared transmission data for crystalline phase pentacene²⁴ and tetracene neutral were available^{25,26} as a basis for comparison to our matrix isolated values.

Through the use of a dual beam apparatus, both the electronic and infrared spectra of a matrix-isolated sample could be collected in these studies. As a result, the assignment of new infrared absorbance features was facilitated by correlation with known electronic features. The PAH cations have characteristic electronic absorbance features in the visible region unlike the neutral molecules whose features lie in the UV region. Identification of a known PAH cation electronic absorbance feature was initiated by comparing the neutral spectrum to the spectrum collected after passing the neutral through an electron beam. Identification of the neutral electronic features in the UV region for pentacene and tetracene was verified by previous work reported by Klevens and Platt who had examined a series of catacondensed hydrocarbons²⁷.

There were no previous studies of the electronic absorption spectrum for pentacene cation. Verification of the assignment of the visible feature to pentacene cation was assisted by the photoelectron (PE) spectrum previously measured and assigned by Schmidt²⁸ for pentacene neutral. The order of orbitals shown by a PE spectrum are that of the cation²⁹ and the difference between the first and second

ionization potentials (1.31 eV) corresponded to the first electronic absorption band ($S_1 \leftarrow S_0$) observed for pentacene cation.

Both PE and UV/Visible spectroscopic studies of tetracene cation were reported. Figure 7(a) is the electronic absorption spectrum for tetracene cation collected by Shida using γ -ray ionization in a solid s-butylchloride matrix at 77K. The band origin at 395 nm³⁰ reported by Shida reflected excellent agreement with band origins reported in previous work at 392.6³¹ and 394 nm³². In addition, the first electronic absorption band ($S_1 \leftarrow S_0$) at 865 nm was in excellent agreement with the corresponding PE spectrum for tetracene neutral. The difference between the first and second ionization potentials for tetracene was 1.44 eV²⁸ (861 nm).

In the course of our study of pentacene and tetracene cations, new infrared absorption bands were observed that did not correlate with the cation features and were subsequently identified as anions. Previous spectroscopic studies on pentacene and tetracene anion involved electronic absorption investigations. Buschow *et al* studied³³ the electronic absorption spectrum of "free" pentacene anion in 2-methyltetrahydrofuran (MTHF, C₅H₁₀O) while examining the association of aromatic hydrocarbon negative ions with alkali ions. A band origin at 11,500 cm⁻¹ (870 nm) was reported, which agreed well with later work by Shida and Iwata who reported³⁴ a band origin at 884.6 nm. The electronic absorption spectrum for tetracene anion was also previously collected and is shown in Figure 7(b). Examination of the tetracene electronic absorption features depicted in Figure 7 indicated that it may be hard to distinguish between the two in electronic absorption investigations since the features are similar. The observation of anions, as well as cations, in the infrared absorption studies of matrix-isolated PAH ions

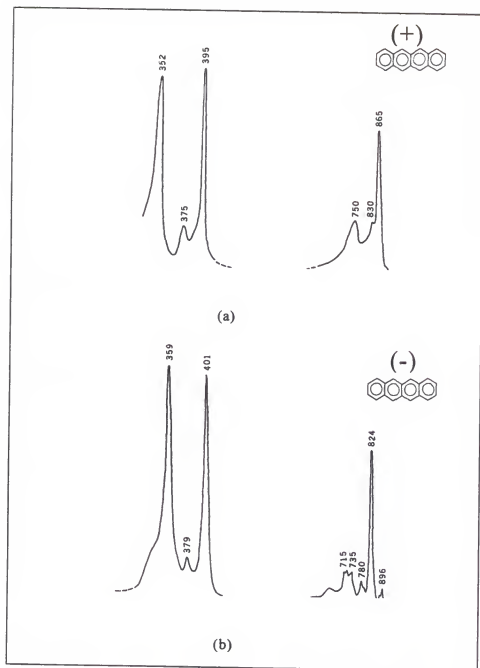


Figure 7. Electronic spectra of tetracene ions. (a) Tetracene cation in s-butylchloride matrix (77 K). (b) Tetracene anion in methyl tetrahydrofuran matrix (77 K). Adapted from Shida³⁰.

added another dimension to the hypothesis that PAHs are responsible for the UIR emission.

B. Experimental

Figure 8 shows the schematic diagram of the chamber used to deposit matrix isolated PAH molecules. By resistively heating a wire wound around a quartz capsule containing a PAH, the solid sample was sublimed, mixed with the isolant Ar gas and deposited on a BaF₂ cold window (12K). Figure 9 illustrates the configuration of the cold window at the end of a closed-cycle, helium cryostat finger (Displex 202, APD). A Pt/Au thermocouple (Air Products, APD E Digital Temperature Indicator/Controller) placed between the window holder and the cold finger measured temperature.

The transparency range of the BaF₂ window is 200 nm to 14 μ m, which was necessary to sequentially collect the UV/Visible and IR spectra of the same sample matrix. A Cary 17 spectrophotometer took the UV/Visible spectra with 0.2 to 1.0 nm resolution and over the range 240 to 1000 nm. A Nicolet 7199 Fourier transform infrared (FT-IR) spectrometer recorded the IR spectra collecting 500 scans at 1 cm⁻¹ resolution. The cryostat/window was positioned in the Cary sample compartment with an IR detector placed below the compartment. When the cryostat was rotated 90°, the IR beam was directed from the FTIR, through the cold window and focused on a 77 K Hg-Cd-Te (MCT) detector with a series of mirrors. The "cross beam" arrangement was used to correlate known UV/Visible features with newly observed IR features of PAH ions.

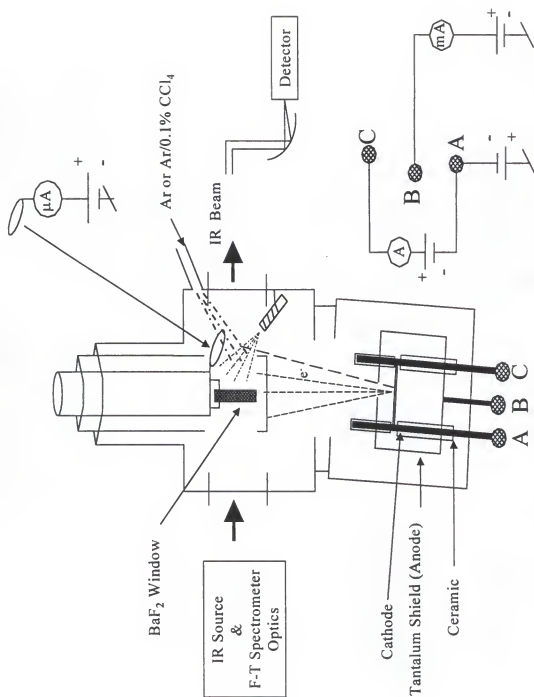


Figure 8. Experimental setup for the preparation of PAH ions in a 12K Ar matrix using a low energy electron impact technique.

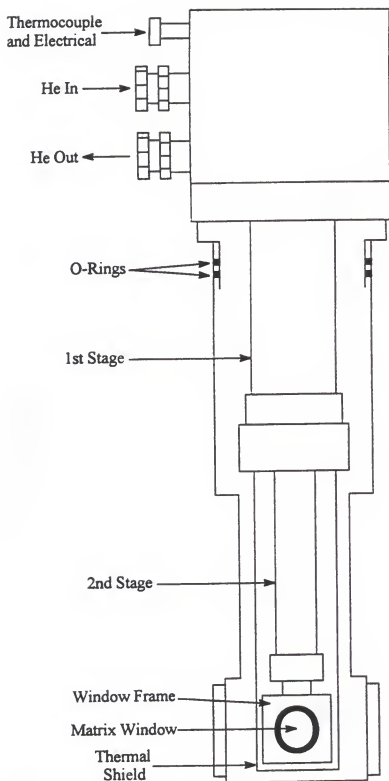


Figure 9. Closed-cycle helium cryostat showing matrix window in copper holder (Displex 202, APD).

Figure 8 also includes details of the electron impact source used to generate PAH ions. Süzer and Andrews first utilized the design in 1988³⁵ for matrix-isolation FTIR studies of the H₂O system and observed the OH radical, OH⁻ and Ar_nH⁺. Electrons were sputtered from 0.1 mm diameter tungsten wire rolled into 15 spiral loops of approximately 4 mm in diameter. The tungsten cathode was placed 3.5 mm from the tantalum plate anode that had a 3 mm diameter exit hole in the center. The electrical circuits used to control the electron beam are also shown in Figure 8. A d.c. cathode-to-anode potential [$U_B(\text{cathode}) = -50\text{--}160\text{ V}$; $U_A(\text{anode}) = 0\text{--}30\text{ V}$] accelerated the electrons inside the electron gun. An o-ring electrode, placed next to the deposition window at an approximately 45° angle and with an $\sim +50\text{ V}$ [U_o] potential, accelerated the electron beam towards the window. The sample mixture was then intersected with the low energy electron beam and deposited on the cold cryostat window held at 12K.

The current at the o-ring was also monitored in order to determine electron production, which in effect measured the degree of positive ion production. With the electron gun on and no sample being deposited, the current at the electron gun was $\sim 1\text{ }\mu\text{A}$. With the e-beam on and Ar/0.1% CCl₄/PAH added, the current at the o-ring measured 20–40 μA . CCl₄ (0.1%) was added to the Ar as a vapor phase ionization enhancer and matrix phase electron trap. Adding CCl₄ increased the production of cations due to charge transfer reactions, but competed with the production of PAH anions. Therefore, removing CCl₄ from the Ar mixture and generating the e-beam during PAH deposition was a method for distinguishing the infrared absorption anion features from the cation.

For neutral pentacene and tetracene samples, the infrared and electronic absorption spectra were obtained by depositing Ar (no CCl_4) and sublimed PAH with the e-beam disengaged. When the Ar/0.1% CCl_4 mixture was deposited with the PAH sample and the e-beam activated, the observed absorption features corresponded to PAH neutral, cation and anion. However, the anion features, as previously mentioned, were weak due to competition from the CCl_4 and its electron impact products. The behavior of the cation bands upon photolysis by a medium pressure 100 W Hg lamp also helped in their identification. By subtracting the IR spectrum collected after photolysis from the spectrum obtained before photolysis, the bands corresponding to PAH cation (and very small anion features) could be observed as positive features.

Varying concentrations of cation were produced by the following methods: photolysis of the matrix, changing the concentration of CCl_4 in the Ar bulb, changing e-beam parameters and changing the deposition pressure of the Ar mixture. The intensities of the newly observed IR features were then plotted versus the intensity of the corresponding feature in the UV/Visible spectrum and verified the assignment of the IR absorption features. PAH anion features, as mentioned previously, were identified by their increased intensity ratios versus the cation peaks when CCl_4 was removed from the Ar mixture. The PAH anions also decreased in intensity upon photolysis, so the change in intensity ratio versus cation bands upon removing CCl_4 was critical in the identification of the anions.

C. Pentacene Cations and Anions

1. Electronic Spectra

With the e-beam disengaged and no CCl_4 added to the Ar isolant gas, the electronic absorption spectrum of pentacene neutral was obtained. The $S_1 \leftarrow S_0$ and $S_2 \leftarrow S_0$ band origins at 559.7 and 422.2 nm, respectively, were observed as seen in Figure 10. The band origins had been assigned to 585 and 429 nm in previous measurements of pentacene neutral in n-heptane solution²⁷.

The assignment of the pentacene cation electronic absorption bands (Figure 11) was aided by Schmidt's PE spectroscopic results²⁸. The ionization energies and electronic states of the cation are presented in Table 1. The energy of the lowest transition, ${}^2A_u \leftarrow {}^2B_{2g}$, of 1.31 eV²⁸ is in excellent agreement with the 954.1 nm band (1.30 eV) assigned to pentacene cation. The sidebands at 960.9, 967.5 and 984.0 nm are site bands for the $S_1 \leftarrow S_0$ band origin.

The band origin in this work at 882.2 nm, shown in Figure 11, increased in intensity as the concentration of CCl_4 was decreased in the Ar mixture. At concentrations greater than 0.1% CCl_4 , no band at 882.2 nm was observed. Figure 12 illustrates the increase in intensity of the 882.2 feature assigned to pentacene anion when CCl_4 was removed from the Ar isolant gas. Spectrum (A) was obtained after depositing pentacene without CCl_4 in the isolant gas and spectrum (B) was collected with 0.1% CCl_4 in the Ar isolant gas. The top spectrum in Figure 12 represents the subtraction spectrum, A-B, where spectrum B was scaled so that the cation features would disappear. The band at 882.2 nm was assigned to pentacene anion and is in excellent agreement with previous assignments of 870³³ and 884.6 nm³⁴.

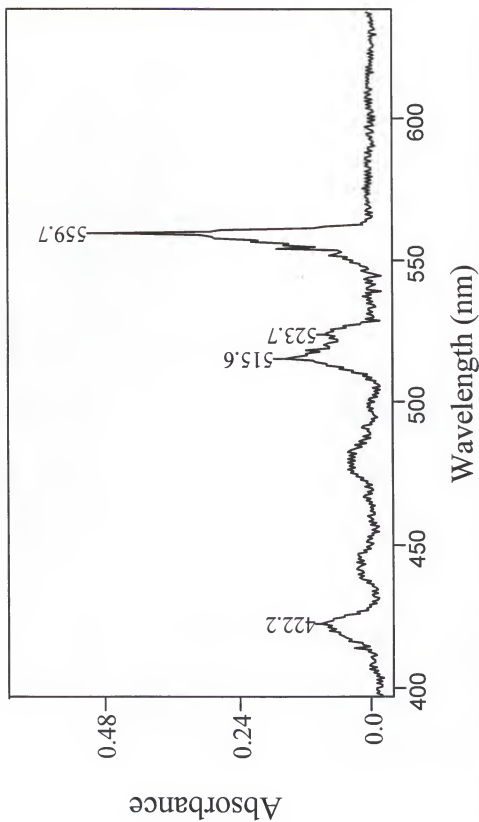


Figure 10. Electronic absorption spectrum of neutral pentacene in Ar at 12K (0.5 nm resolution); no absorption to the red of this region was observed. The spectrum was baseline corrected.

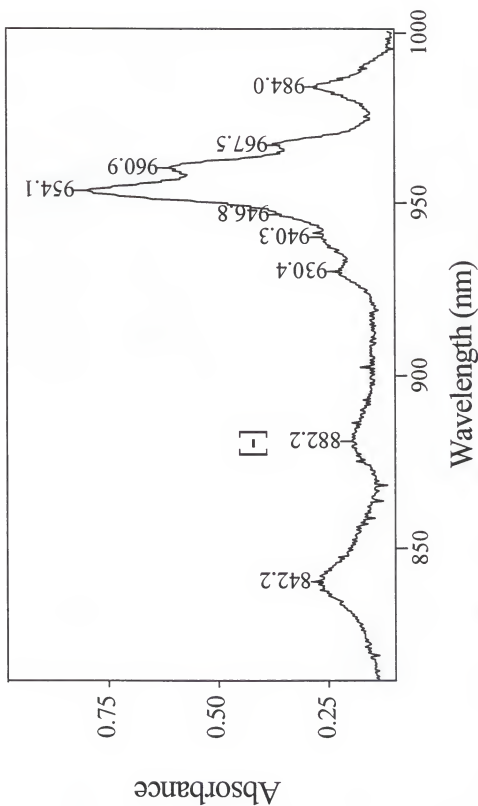


Figure 11. Electronic absorption spectrum of cationic pentacene in Ar with 0.1% CCl_4 at 12K (~ 1 nm resolution). The feature marked by [-] was assigned to pentacene anion. The spectrum was baseline corrected.

Table 1. Vertical ionization potentials (IP) of pentacene and optical absorption transitions for pentacene cations in an Ar matrix at 12K.

State Symmetry ²⁸	IP (eV) ²⁸	Δ IP (eV)	Optical Transition (eV)
$^2B_{2g}$	6.61	1.31 (10568 cm ⁻¹ , 946.3 nm)	1.30 (10481 cm ⁻¹ , 954.1 nm)
2A_u	7.92	1.71 (13795 cm ⁻¹ , 724.9 nm)	Parity forbidden
$^2B_{3g}$	8.32	2.40 (19361 cm ⁻¹ , 516.5 nm)	Parity forbidden
$^2B_{2g}$	9.01	2.78 (22426 cm ⁻¹ , 445.9 nm)	2.91 (23474 cm ⁻¹ , 426.0 nm)
$^2B_{1u}$	9.39	3.19 (25733 cm ⁻¹ , 388.6 nm)	-
2A_u	9.80	3.62 (29202 cm ⁻¹ , 342.4 nm)	Parity forbidden
$^2B_{2g}$	10.23		

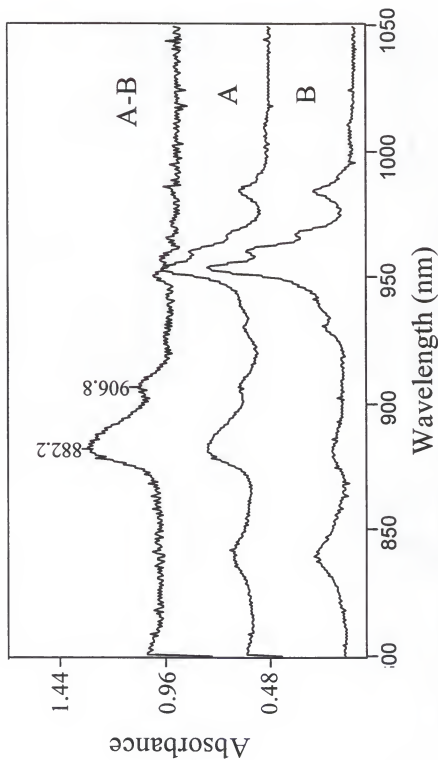


Figure 12. Electronic absorption spectra illustrating the growth of the anion feature at 882.2 nm when CCl_4 was omitted from the Ar isolant gas during deposition of pentacene with the e-beam engaged. Spectrum (A) was pentacene deposited with Ar isolant gas only and the e-beam on. Spectrum (B) was pentacene deposited with Ar and 0.1% CCl_4 isolant gas mixture and the e-beam on. The top spectrum represents the subtraction (A-B) where spectrum (B) was scaled so that the cation features would be removed. Spectra (A) and (B) were baseline corrected.

The electronic absorption feature at 954.1 nm (Figure 11) was the band utilized in the correlation of newly observed infrared absorption bands assigned to pentacene cation. The intensity of the anionic electronic absorption feature at 882.2 nm, however, was not strong enough for a reasonable numerical correlation to be developed. Infrared bands assigned to the pentacene anion molecule were observed to exhibit the same change in intensity ratio versus neutral features as the electronic feature at 882.2 nm.

2. Infrared Spectra

The infrared spectra of matrix isolated pentacene deposited under three conditions in the regions $1600\text{--}1250\text{ cm}^{-1}$ and $1250\text{--}900\text{ cm}^{-1}$ are shown in Figures 13 and 14, respectively. Spectrum (C) in both figures is of neutral pentacene deposited with Ar only as the isolant gas. The most intense bands for neutral pentacene, which are not shown in the spectra, are at $900.1/902.5\text{ cm}^{-1}$ and 731.8 cm^{-1} . Figure 15 is the neutral spectrum depicting the most intense peaks. The peaks assigned to pentacene neutral are in excellent agreement with previous infrared absorption results for crystalline pentacene²⁴. Spectrum (B) in Figures 13 and 14 was obtained during deposition of pentacene with the e-beam engaged and the matrix gas a mixture of Ar and 0.1% CCl_4 . Under these conditions pentacene neutral, cation and a very small amount of anion were deposited. Bands corresponding to CCl_4 and its electron impact products³⁶ are marked with an asterisk (*). Spectrum (A) contains features corresponding to pentacene neutral, cation and anion. The depositing conditions included the e-beam but there was no CCl_4 in the Ar isolant gas. Without CCl_4 , the pentacene anion bands increased considerably compared to spectrum (B), while the ratio of cations to neutrals decreased. The electron

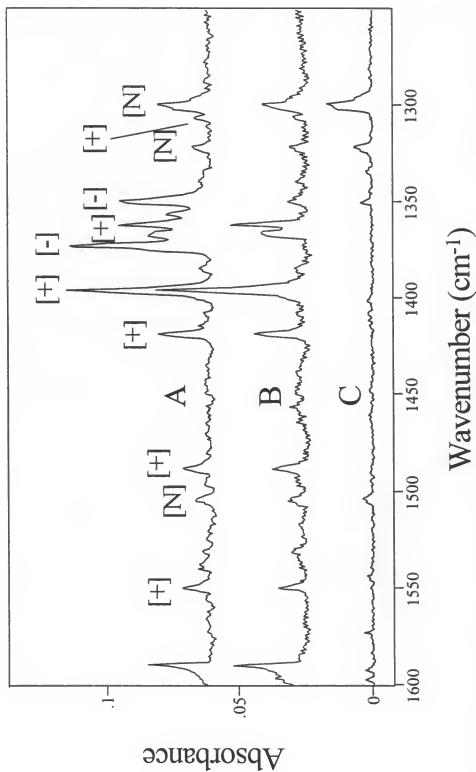


Figure 13 Infrared spectra (1600-1250 cm⁻¹) of pentacene neutrals, cations and anions at 12K. (A) Deposited with e-beam on and Ar gas only. (B) Deposited with e-beam on and Ar gas containing 0.1% CCl₄. (C) Deposited with Ar gas only.

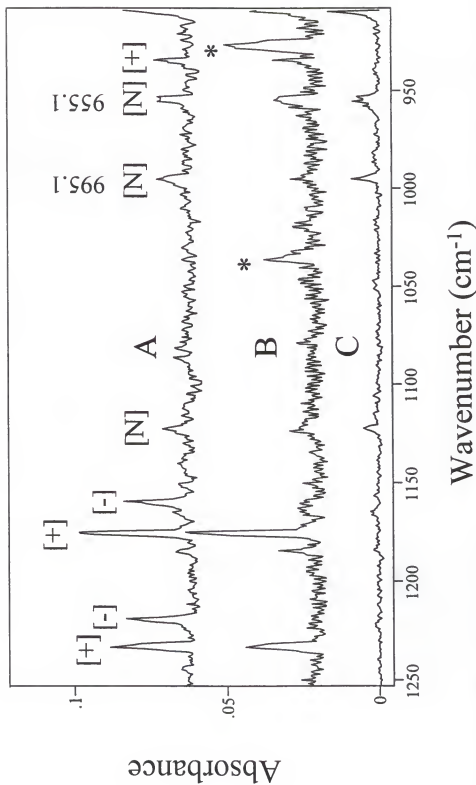


Figure 14 Infrared spectra ($1250\text{-}900\text{ cm}^{-1}$) of pentacene neutrals, cations and anions at 12K. (A) Deposited with e-beam on and Ar gas only. (B) Deposited with e-beam on and Ar gas containing 0.1% CCl_4 . Peaks marked with a (*) are CCl_4 and/or electron impact products of CCl_4 . (C) Deposited with Ar gas only.

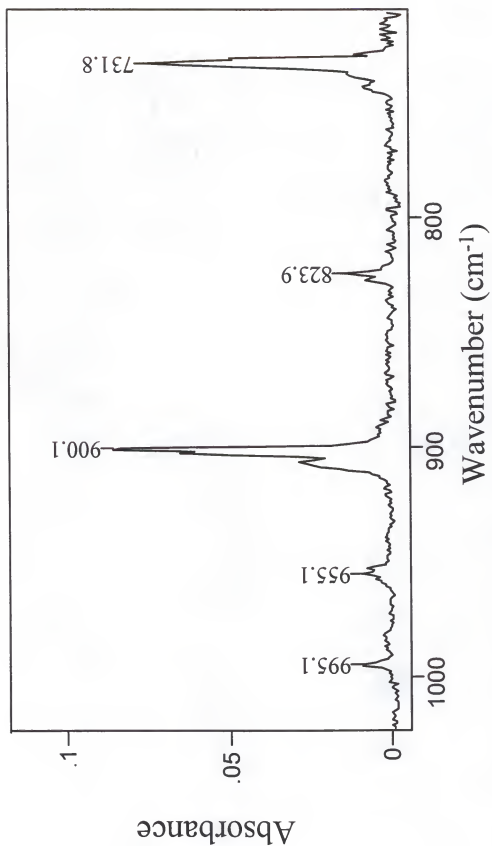


Figure 15. Infrared spectrum for pentacene neutral that shows the most intense features at 900.1/902.5 and 731.8 cm⁻¹.

impact product, Cl, has a higher electron affinity than pentacene, therefore, without Cl to compete for the electrons, a higher yield of pentacene anions was possible.

In addition to their appearance when the neutral pentacene was passed through an electron beam, the pentacene cation features were also differentiated from neutral pentacene based on their behavior upon photolysis with a medium pressure Hg lamp. Figures 16 and 17, spectra (B-C), are the subtraction spectra identifying pentacene cation peaks that decreased after photolysis. Smaller features in the subtraction spectrum not assigned to pentacene cation were assigned to pentacene anion and their identification will be discussed next.

In order to support the assignment of the IR features as pentacene cations, the peaks were correlated with the 954.1 nm electronic absorption feature assigned to pentacene cation. The correlation plots for some of the pentacene cation peaks are shown in Figure 18. Each set of data points corresponds to a sample matrix with different concentrations of pentacene cation. The concentration of pentacene cation was varied by changing the concentrations of elements in the matrix isolant mixture (e.g. CCl_4 , Ar), varying the parameters of the e-beam and/or photolysis of the matrix. The best fit lines for each correlation in Figure 18 had coefficients, R^2 , greater than 0.90. The features listed in the correlation plots, along with the other peaks assigned to pentacene cation, paralleled the intensity of the pentacene cation electronic band at 954.1 nm.

The pentacene anion infrared features were assigned based on their increase in intensity versus pentacene cation upon removal of the CCl_4 from the isolant gas and the fact that they also showed a bleaching behavior upon photolysis. The top spectrum in Figure 19, which corresponds to pentacene anion features, was derived by taking the

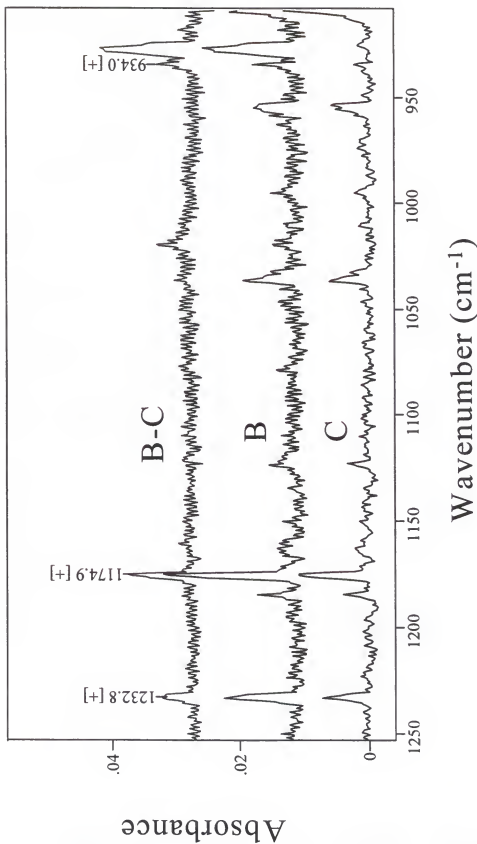


Figure 16. Infrared spectra ($1250\text{--}900\text{ cm}^{-1}$) for determination of pentacene cations. Top spectrum [B-C] showing pentacene cation features [-]. Middle spectrum (B) of pentacene deposited with e-beam on and Ar gas containing 0.1% CCl_4 at 12K before photolysis. Lower spectrum (C) after photolysis.

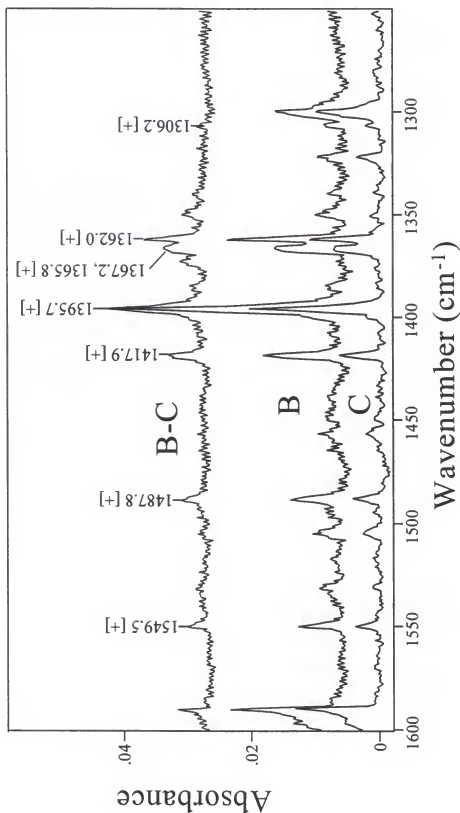


Figure 17. Infrared spectra (1600-1250 cm⁻¹) for determination of pentacene cations. Top spectrum [B-C] showing pentacene cation features [+]. Middle spectrum (B) of pentacene deposited with e-beam on and Ar gas containing 0.1% CCl₄ at 12K before photolysis. Lower spectrum (C) after photolysis.

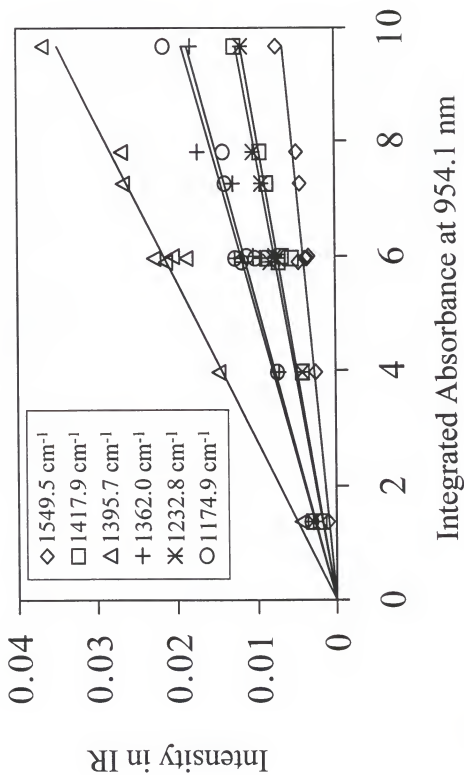


Figure 18. Intensity correlation plot for the 954.1 nm pentacene cation electronic band and newly observed IR bands.

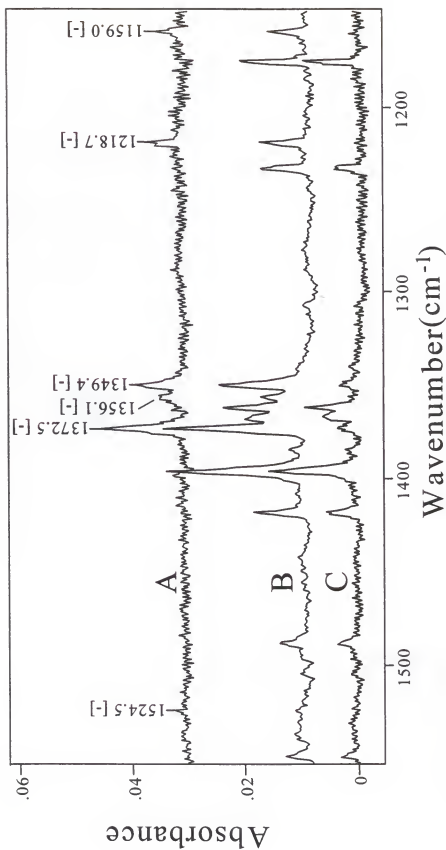


Figure 19. Infrared spectra ($1550\text{--}1150\text{ cm}^{-1}$) for determination of pentacene anions. Top spectrum [A] showing pentacene anion features [-]. Middle spectrum (B) was the subtraction spectrum [before photolysis minus after photolysis] of pentacene deposited with the e-beam on and Ar only at 12K. The relative intensity of the pentacene anion peaks is much higher versus neutrals and cations. Bottom spectrum (C) was the subtraction spectrum [before photolysis minus after photolysis] of pentacene deposited with the e-beam on with Ar gas containing CCl_4 . The relative intensities of pentacene anions is much less than spectrum (B). Subtracting spectrum (C) from spectrum (B) such that the neutral and cation features were removed left the anion features.

difference of two subtraction spectra (before photolysis minus after photolysis) between a sample deposited with CCl_4 (spectrum C) and without CCl_4 (spectrum B). Spectrum C was scaled so that the features corresponding to pentacene cation would be removed from spectrum B and the resultant spectrum (A) corresponded to pentacene anion features that increased in intensity versus the cation bands when CCl_4 was removed from the isolant gas. In addition, IR bands assigned to pentacene anion also tracked the intensity of the electronic band at 882.2 nm.

3. Vibrational Analysis

Tables 2-4 list the frequencies and relative intensities of the IR absorption bands of neutral, cationic and anionic pentacene, respectively. Accompanying the experimental results for each are the theoretical values calculated by Langhoff³⁷. The differentiating characteristic of the cation and anion bands relative to neutral were the positions of the most intense bands. For neutral pentacene, the most intense bands were the out-of-plane CH wagging modes at 731.8 cm^{-1} ($13.7\text{ }\mu\text{m}$) and 900.1 cm^{-1} ($11.1\text{ }\mu\text{m}$). While for the cation and anion, the strongest bands were the in-plane CC stretching modes and the in-plane CH bending modes near 1350 cm^{-1} ($7.4\text{ }\mu\text{m}$) and 1200 cm^{-1} ($8.3\text{ }\mu\text{m}$).

There are some differences between the theoretical and experimental values that should be noted. Theoretical calculations for neutral pentacene predict that the most intense peak is in the CH stretch region at 3078.5 cm^{-1} . Two factors have been proposed to contribute to the discrepancy³⁷. First, based on preliminary gas phase results for naphthalene, matrix effects were proposed to reduce the relative intensity of the CH

Table 2. Vibrational analysis of neutral pentacene.

Experimental			Theory(B3LYP/4-31G) ^a		
ν (cm ⁻¹) ^b	Relative Intensity ^b	ν (cm ⁻¹) ^c	Symmetry	ν (cm ⁻¹)	Intensity (km/mol) ^d
3089.8	0.07	3072	b _{2u}	3078.5	142.8 (1.00)
3066.2	0.12		b _{1u}	3053.9	81.5 (0.57)
3053.7	0.09		b _{2u}	3048.5	5.3 (0.04)
			b _{1u}	3044.9	53.2 (0.37)
			b _{1u}	3043.1	9.4 (0.07)
			b _{1u}	3042.5	5.2 (0.04)
3039.7	0.10	3043	b _{2u}	3038.9	2.6 (0.02)
1634.3	0.07	1627	b _{1u}	1623.1	11.6 (0.08)
1597.2	0.03	1595			
1572.6	0.03	1570			
		1557			
1543.7	0.02	1539			
1504.7	0.05	1499	b _{2u}	1503.1	2.4 (0.02)
1447.3	0.02	1444			
1350.4	0.05	1345			
1321.9	0.07	1325	b _{2u}	1331.8	11.5 (0.08)
1298.8	0.21	1299	b _{1u}	1290.8	24.1 (0.17)
		1222			
1184.0	0.02	1184	b _{1u}	1198.0	2.4 (0.02)
1164.3	0.03	1160			
			b _{2u}	1132.5	2.9 (0.02)
1121.8	0.06	1117	b _{1u}	1117.7	5.5 (0.04)
995.1	0.10	991	b _{2u}	991.8	3.7 (0.03)
954.6/ 955.1	0.14	960	b _{3u}	961.7	10.7 (0.07)
900.1/ 902.5	1.00	909	b _{3u}	914.5	102.4 (0.72)
		892	b _{1u}	911.5	2.0 (0.01)
823.9/ 826.3	0.16	845	b _{3u}	829.2	19.4 (0.14)
		762			
731.8	0.86	734	b _{3u}	735.4	73.4 (0.51)

^aLanghoff²⁷. Frequencies scaled by 0.958.^bThis work. Ar matrix at 12K.^cColanelli *et al*²⁴. Crystalline phase.^dRelative intensities in parentheses.

Table 3. Vibrational analysis of cationic pentacene.

Experimental	Theory(B3LYP/4-31G) ^a		
$\nu^{b,c}$ (cm ⁻¹)	Sym	ν (cm ⁻¹)	Intensity ^c (km/mol)
1549.5 (0.18)	b _{2u}	3098.8	50.6 (0.05)
	b _{1u}	3086.4	14.7 (0.02)
	b _{1u}	1586.8	27.7 (0.03)
	b _{2u}	1517.6	246.8 (0.26)
1487.8 (0.21)	b _{2u}	1488.7	499.1 (0.53)
1417.9 (0.36)			
1395.7 (1.00)	b _{2u}	1390.4	205.6 (0.22)
	b _{2u}	1379.0	145.3 (0.15)
1367.2/	b _{2u}	1359.2	946.0 (1.00)
1365.8(0.04)			
1362.0(0.56)	b _{1u}	1296.2	38.0 (0.04)
1306.2 (0.10)	b _{2u}	1236.9	179.8 (0.19)
1232.8 (0.39)			
1174.9 (0.48)	b _{2u}	1186.7	108.6 (0.11)
	b _{2u}	1173.7	84.9 (0.09)
	b _{3u}	980.1	14.3 (0.02)
934.0 (0.15)	b _{3u}	941.5	75.2 (0.08)
	b _{3u}	862.3	16.8 (0.02)
	b _{3u}	753.7	92.6 (0.10)

^aLanghoff³⁷. Frequencies scaled by 0.958.^bThis work. Ar matrix at 12K.^cRelative intensities in parentheses.

Table 4. Vibrational analysis of anionic pentacene.

Experimental	Theory(B3LYP/4-31G) ^a		
$\nu^{b,c}$ (cm ⁻¹)	Irrep	ν (cm ⁻¹)	Intensity (km/mol) ^c
	b _{2u}	3048.8	402.4 (0.31)
	b _{1u}	3031.0	219.0 (0.17)
	b _{1u}	3014.7	158.4 (0.12)
1524.5 (0.02)	b _{2u}	1513.5	355.9 (0.28)
	b _{2u}	1487.2	132.1 (0.10)
1372.5 (1.00)	b _{2u}	1373.2	200.7 (0.16)
1356.1 (0.28)	b _{2u}	1363.2	194.8 (0.15)
1349.4 (0.65)	b _{2u}	1342.1	1293.4 (1.00)
	b _{1u}	1280.0	24.3 (0.02)
1218.7 (0.33)	b _{2u}	1225.2	148.3 (0.11)
1159.0 (0.32)	b _{2u}	1175.5	70.2 (0.05)
	b _{2u}	1007.1	14.0 (0.01)
	b _{3u}	907.7	17.7 (0.01)
845.2 (0.10)	b _{3u}	849.5	132.8 (0.10)
	b _{3u}	774.8	14.5 (0.01)
	b _{2u}	727.8	19.0 (0.01)
	b _{3u}	713.6	62.7 (0.05)

^aLanghoff³⁷. Frequencies scaled by 0.958.^bThis work. Ar matrix at 12K.^cRelative intensities in parentheses.

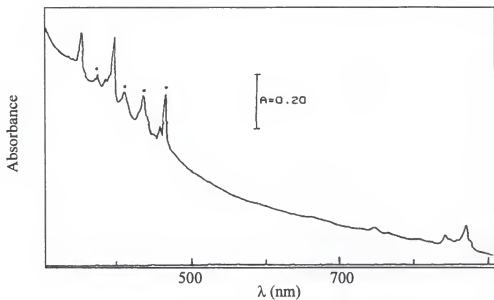
stretch in matrix isolation experiments by a factor of 2. In addition, the small basis set, 4-31G, was proposed to overestimate the intensity of the CH stretch by another factor of 2. If the theoretical relative intensities were scaled to the predicted feature at 914.5 cm^{-1} as the most intense band, then many of the theoretical relative intensities would be more in line with experimental values. Overall, with the exception of the CH stretch region, the agreement between theoretical and experimental values for pentacene neutral is good.

A primary discrepancy between theory and experiment for pentacene cation was the incorrect assignment of intensities by theory to the b_{2u} modes between 1359 and 1390 cm^{-1} . However, if the relative intensities of the experimental features were calculated relative to the combined intensities of experimental values between 1362 and 1396 cm^{-1} , the agreement with theoretical was reasonable. A similar discrepancy in relative intensities was apparent for the pentacene anion experimental and theoretical results. Based on results obtained with naphthalene anion, the 4-31G basis set overestimated theoretical intensities by $\sim 20\%$ compared to using the 6-31G* basis set³⁷. In addition, the b_{2u} bands between 1342 and 1374 cm^{-1} had intensity ratios incorrectly apportioned which were similar to the pentacene cation results.

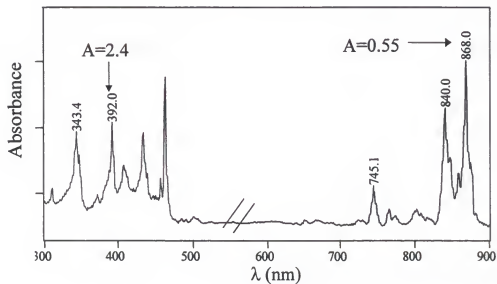
D. Tetracene Cations and Anions

1. Electronic Spectra

Figure 20 (a) shows the electronic absorption spectrum collected by Andrews *et al* after depositing tetracene with excess Ar at 20K with concurrent vacuum-ultraviolet radiation³¹. The peaks marked with a dot were the precursors to irradiation, tetracene neutral, and the unmarked peaks were identified as tetracene cation. Spectrum (b) is the electronic absorption obtained for this work. The band origin at 392.0 nm , assigned to



(a)



(b)

Figure 20. Electronic spectra of tetracene neutral and cation. (a) Ar at 20K deposited with concurrent vacuum-ultraviolet radiation. Precursor peaks collected before UV radiation and corresponding to neutral tetracene are marked with a dot. Adapted from Andrews *et al.*³¹ (b) Deposited with Ar/0.1% CCl₄ and e-beam engaged, this work. The spectrum was baseline corrected.

tetracene cation, shows excellent agreement with previous work with band origins at 392.6³¹, 395³⁰, and 394 nm³². In addition, the band origin at 868.0 nm was in excellent agreement with previous PE spectroscopic results that reported the ${}^2A_u \leftarrow {}^2B_{2g}$ ($D_1 \leftarrow D_0$) transition as 1.44 eV or 861 nm²⁸.

In addition to their appearance when tetracene neutral (mixed with Ar and 0.1% CCl₄) was passed through an electron beam, tetracene cation features were also identified by their bleaching behavior upon photolysis by a medium pressure Hg lamp. The subtraction spectrum (before photolysis minus after photolysis) shows peaks identified as due to the tetracene cation in Figure 21. The tetracene cation spectrum, collected by Shida *et al* using γ -ray ionization in a solid s-butylchloride matrix at 77K³⁰ is shown in Figure 7(b) and is in excellent agreement with the electronic features assigned to tetracene cation in Figure 21. The band origin at 392.0 nm is the electronic absorption feature utilized in the correlation of newly observed infrared absorption features identified as tetracene cation.

No peaks in the electronic absorption spectrum were identified as tetracene anion, however, the possibility for overlap with the tetracene cation features cannot be ignored. As noted earlier, the electronic absorption spectrum for tetracene neutral and cation are very similar. In order to minimize possible error due to anion interference, the data used for the correlation of infrared peaks with the 392.0 nm electronic absorption feature were collected from runs where CCl₄ was added to the Ar matrix gas.

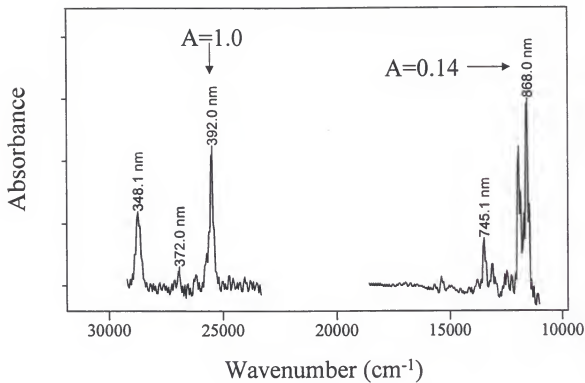


Figure 21. Electronic spectrum of tetracene cation. Each region is a subtraction spectrum (after photolysis minus before photolysis) where positive features correspond to tetracene cation.

2. Infrared Spectra

The infrared spectra of matrix isolated tetracene deposited under three conditions in the spectral regions 1600-1250 and 1250-750 cm^{-1} are shown in Figures 22 and 23, respectively. Spectrum (C) represents a deposit with Ar only and corresponds to tetracene neutral features. The most intense bands for tetracene neutral at 742.9/740.5 and 895.3 cm^{-1} are shown in Figure 24. Spectrum (B) was tetracene deposited with Ar/0.1% CCl_4 and the e-beam activated. The deposit generated, in addition to tetracene neutral, both cations and anions. However, with CCl_4 added to the matrix gas the intensity of the anion features is very low. Spectrum (C) represents a deposit under the same conditions as (B) except no CCl_4 was added to the mixture. The features that increased in relative intensity, versus cation features, were identified as anions.

Identification of tetracene cation features was also accomplished by tracking the behavior of those features that decreased upon photolysis. Figure 25 shows an example of the cation spectrum (B-C) generated by subtracting the before photolysis spectrum (B) from the after photolysis spectrum (C). The tetracene anion features also decreased upon annealing, but as discussed previously, they were easily differentiated from the cation features by changing the concentration of CCl_4 in the Ar gas. The smaller features in the top spectrum not assigned to tetracene cation are anion features that will be discussed next.

In order to support the assignment of the IR features as tetracene cations, the peaks were correlated with the 392.0 nm electronic absorption feature assigned to tetracene cation. The correlation plots for some of the tetracene cation peaks are shown in Figure 26. Each set of data points corresponds to a sample matrix with different

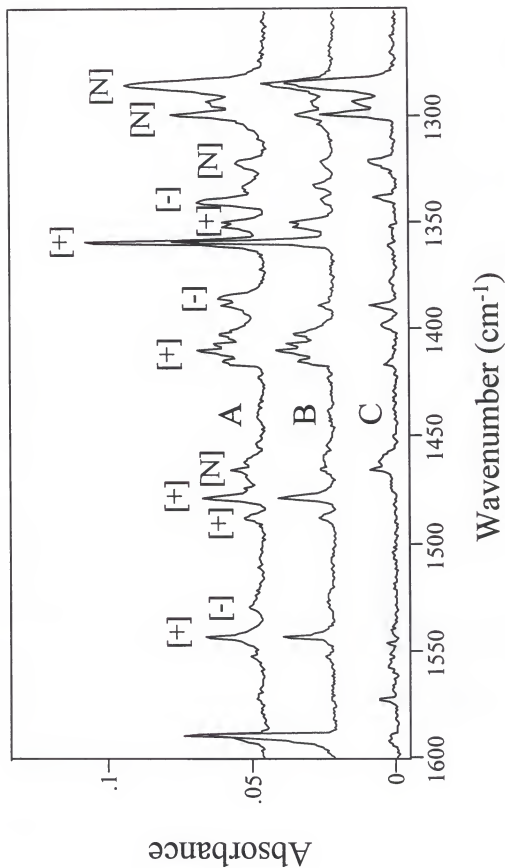


Figure 22. Infrared spectra ($1600\text{--}1250\text{ cm}^{-1}$) of tetracene neutrals, cations and anions at 12K. (A) Deposited with the e-beam on and Ar only. (B) Deposited with the e-beam on and Ar gas containing 0.1% CCl_4 . (C) Deposited with Ar only.

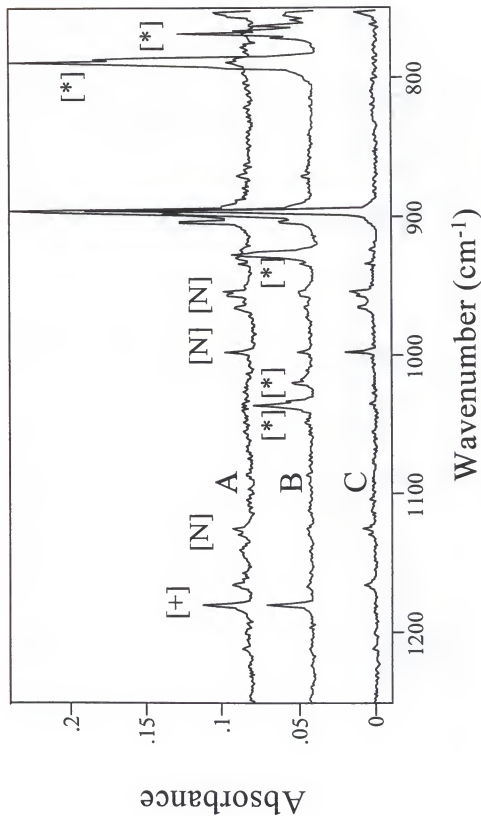


Figure 23. Infrared spectra ($1250\text{--}750\text{ cm}^{-1}$) of tetracene neutrals, cations and anions at 12K. (A) Deposited with the e-beam on and Ar only. (B) Deposited with the e-beam on and Ar gas containing 0.1% CCl_4 . Peaks marked with a (*) are CCl_4 and/or electron impact products. (C) Deposited with Ar only.

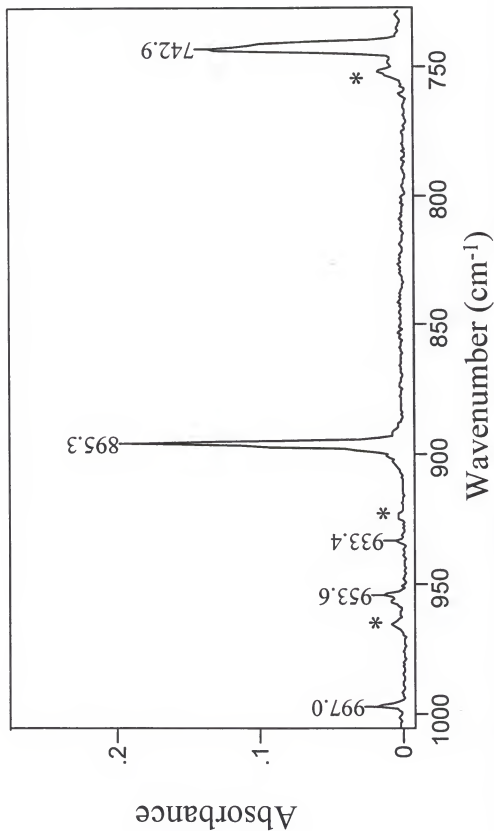


Figure 24. Infrared spectrum for neutral tetracene deposited with Ar only isolant gas at 12K showing the most intense features at 742.9/740.5 and 895.3 cm⁻¹. The peaks marked with an asterisk (*) correspond to naphthalenequinone, which is a compound used to synthesize tetracene and which was present as a contaminant in the tetracene sample.

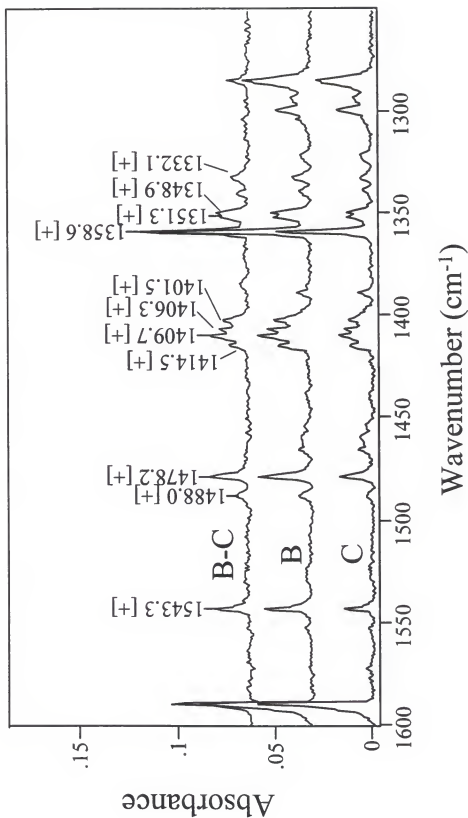


Figure 25. Infrared spectra (1600-1250 cm^{-1}) for determination of tetracene cations. (A) Subtraction spectrum [B-C] showing tetracene cation features [+]. (B) Spectrum before photolysis of tetracene deposited with e-beam and Ar/0.1% CCl_4 at 12 K. (C) Spectrum after photolysis.

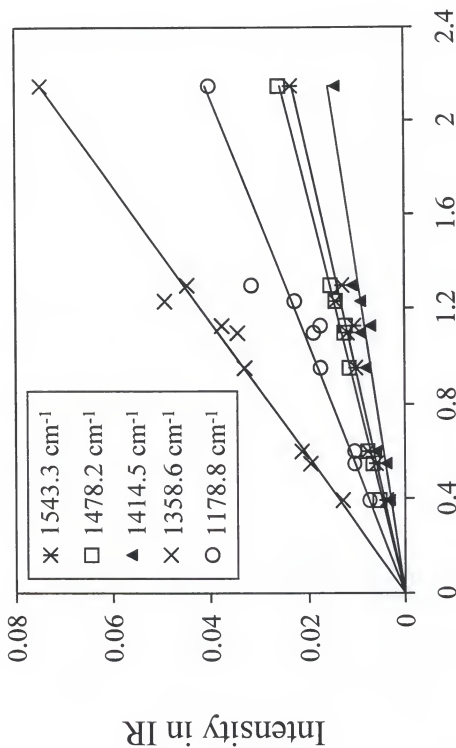


Figure 26. Intensity correlation plot for the 392.0 nm tetracene cation electronic band and newly observed IR bands.

concentrations of tetracene cation. The concentration of tetracene cation was varied by changing the concentrations of elements in the matrix isolant mixture (e.g. CCl_4 , Ar), varying the parameters of the e-beam and/or photolysis of the matrix. The best fit lines for each correlation in Figure 26 had coefficients, R^2 , greater than 0.90. The features listed in the correlation plots, along with the other peaks assigned to tetracene cation, paralleled the intensity of the tetracene cation electronic band at 392.0 nm.

The tetracene anion infrared features were assigned based on their increase in intensity versus tetracene cation upon removal of the CCl_4 from the isolant gas and the fact that they also showed a bleaching behavior upon photolysis. The intensity of the tetracene anion features versus tetracene cation was less than the corresponding ratio for pentacene anion. The observation was in accordance with the electron affinities of pentacene and tetracene which are 1.2 and 0.95 eV, respectively. Unlike the pentacene anion infrared features, there was no apparent tetracene anion electronic absorption feature whose intensity could be tracked relative to the infrared features.

3. Integrated Intensities of Infrared Transitions

In order to calculate emission spectra at various energetic or thermal approximations corresponding to interstellar space, the integrated intensities of the infrared features are needed. Based on the absolute intensity of a UV/Visible feature for tetracene neutral and cation, the integrated intensities for the neutral and cationic infrared features were calculated. The calculation is possible due to the dual beam capabilities of the apparatus that allowed the UV/Visible and IR spectra to be collected for the same sample matrix.

The determination of infrared band intensities for neutral and cationic tetracene followed a three-step procedure. First, the electronic absorption spectra of tetracene neutral and cation were recorded in boric acid. Using a technique developed by Khan and Khanna³⁸, the room temperature solid boric acid/tetracene film was ionized by photolysis with a mercury lamp. The production of tetracene cation was through two-color photoionization. The T_1 triplet state of tetracene neutral is sufficiently close to the ground state D_0 of tetracene cation for a two-color photoionization production of tetracene cations. With the assumption that each depleted neutral molecule became a cation, the following equation holds true,

$$\epsilon_{\max}^+ = (\Delta A_{\max}^+ / \Delta A_{\max}^0) \epsilon_{\max}^0 \quad (1)$$

where ΔA_{\max}^0 and ΔA_{\max}^+ were the changes in absorbance after photolysis, and ϵ_{\max}^0 and ϵ_{\max}^+ were the molar absorption coefficients for neutral and cationic tetracene, respectively.

Second, a value of $\epsilon_{\max}^0(472 \text{ nm})_{\text{heptane}} = 14000 \text{ M}^{-1}\text{cm}^{-1}$ ¹⁷ was used together with corrections for band width (fwhm) and refractive index differences (and assuming the integral band oscillator strength does not change with medium and/or phase) to find the analogous $\epsilon_{\max}^0(472 \text{ nm}) \approx 7000 \text{ M}^{-1}\text{cm}^{-1}$ in boric acid. Photolysis of the boric acid film (10 min) gave a $[\Delta A_{\max}^+(395 \text{ nm}) / \Delta A_{\max}^0(478 \text{ nm})]$ ratio = 4.2. Substitution into (1) gave $\epsilon_{\max}^+(395 \text{ nm})_{\text{BA}} \approx 29400 \text{ M}^{-1}\text{cm}^{-1}$. The same electronic transition was shifted to 392 nm (fwhm $\approx 260 \text{ cm}^{-1}$) in Ar and the calculated $\epsilon_{\max}^+(392 \text{ nm})_{\text{Ar}} = 85300 \text{ M}^{-1}\text{cm}^{-1}$ was comparable to the value of $53300 \text{ M}^{-1}\text{cm}^{-1}$ found by Kimura *et al* for the 394 nm band of tetracene cation in sulfuric acid³².

Finally, the cation electronic molar absorption coefficient and the slopes of the visible/IR correlation plots are used to determine the IR ϵ^+_{\max} values,

$$\epsilon^+_{\max}(\text{IR}_i)_{\text{Ar}} = S_i \epsilon^+_{\max}(392 \text{ nm})_{\text{Ar}}, \quad (2)$$

where the S_i were the slopes of the intensity correlation plots. The most intense feature at 1358.1 cm^{-1} will be used as an example. With $S_{1358.1} = 0.0370$ and substitution into (2), the $\epsilon^+_{\max}(1358.1 \text{ cm}^{-1})$ value is equal to $3156 \text{ M}^{-1}\text{cm}^{-1}$. Substitution into the equation for the integral intensity of an IR band,

$$\begin{aligned} I_i &= 2.303 \int \epsilon^+_{\max}(\text{IR}_i)_{\text{Ar}} dv \\ &\approx 2.303 \epsilon^+_{\max}(\text{IR}_i)_{\text{Ar}} \Delta v_{1/2} \end{aligned} \quad (3)$$

gave $I_{1358.1} = 182 \text{ km/mol}$.

The integral intensities of tetracene neutral were calculated with the assumption that the refractive indices for heptane and solid Ar are similar. Using $\epsilon^0_{\max}(472 \text{ nm})_{\text{heptane}} = 14000 \text{ M}^{-1}\text{cm}^{-1}$ and the fwhm ratio (≈ 1.56),

$$\epsilon^0_{\max}(461.8 \text{ nm})_{\text{Ar}} = [\Delta v_{1/2}(472 \text{ nm})_{\text{heptane}}] / [\Delta v_{1/2}(461.8 \text{ nm})] \epsilon^0_{\max}(472)_{\text{heptane}} \quad (4)$$

$\epsilon^0_{\max}(461.8 \text{ nm})_{\text{Ar}} = 21800 \text{ M}^{-1}\text{cm}^{-1}$. The integral intensities of the neutral tetracene IR bands were then calculated using (3) and

$$\epsilon^0_{\max}(\text{IR})_{\text{Ar}} = \epsilon^0_{\max}(461.8 \text{ nm})_{\text{Ar}} [A^0_{\max}(\text{IR})_{\text{Ar}} / A^0_{\max}(461.8 \text{ nm})_{\text{Ar}}] \quad (5)$$

where $A^0_{\max}(\text{IR})_{\text{Ar}}$ and $A^0_{\max}(461.8 \text{ nm})_{\text{Ar}}$ were absorbances for the IR and 461.8 nm electronic absorption band for neutral tetracene, respectively. Table 5 and Table 6 list the integrated intensities calculated for the experimental tetracene neutral and cationic bands, respectively.

4. Vibrational Analysis

Tables 5, 6 and 7 give the vibrational assignments and comparative theoretical work for tetracene neutral, cation and anion, respectively. Tetracene neutral and cationic results include theoretical calculations by Langhoff³⁷. In addition, the previous experimental results for tetracene neutral²⁵ are presented for comparison. The theoretical calculations for tetracene anion were performed using Gaussian 94^{®39} at the B3LYP/4-31G level of theory. Langhoff's calculations for tetracene neutral and cation were repeated with essentially identical results in order to insure the proper treatment of the anionic molecule.

The differentiating characteristic for the cation and anion bands relative to the neutral bands were the positions of the most intense bands. For neutral tetracene, the most intense bands were the out-of-plane CH wagging modes at 742.9 cm^{-1} ($13.4\text{ }\mu\text{m}$) and 895.3 cm^{-1} ($11.2\text{ }\mu\text{m}$). While for the cation and anion, the strongest bands were the in-plane CC stretching modes at 1358.6 cm^{-1} ($7.4\text{ }\mu\text{m}$) and 1339.9 cm^{-1} ($7.5\text{ }\mu\text{m}$), respectively.

As was noted for pentacene, there are some differences between the theoretical and experimental values that should be noted. Theoretical calculations for neutral tetracene predict that the most intense peak is in the CH stretch region at 3078.1 cm^{-1} . Again, the small basis set, 4-31G, and a matrix effect on the experimental CH stretch intensities are proposed³⁷ to be somewhat responsible for the discrepancy. The experimental integrated intensities, with the exception of the CH stretch region, are approximately a factor of 2 greater than the theoretical values for the most intense features. Langhoff noted the same difference for results on the naphthalene molecule³⁷.

Table 5. Vibrational analysis of neutral tetracene.

Experimental		Theory(B3LYP/4-31G) ^a			
ν (cm ⁻¹) ^b	Intensity ^b (km/mol) ^c	ν (cm ⁻¹) ^d	Irrep	ν (cm ⁻¹)	Intensity (km/mol) ^e
3095	10 (0.06)	3084	b _{2u}	3078.1	120.5 (1.00)
3075	13 (0.08)		b _{1u}	3063.7	68.9 (0.57)
3062	20 (0.12)	3062	b _{1u}	3043.3	15.6 (0.13)
3054	26 (0.16)	3047	b _{1u}		
1640.6/ 1636.7	8 (0.05)	1632	b _{1u}	1625.7	9.1 (0.08)
1546.1	3 (0.02)	1542	b _{2u}	1536.0	2.8 (0.02)
1465.6	5 (0.03)	1462	b _{2u}	1469.6	3.4 ((0.03)
1415.9	3 (0.02)	1410			
1388.9	7 (0.04)	1389		1392.3	4.4 (0.04)
1337.8	6 (0.035)	1331	b _{2u}	1337.5	6.6 (0.05)
1298.8	15 (0.09)	1298			
1292.5	8 (0.05)	1292	b _{1u}	1292.5	4.4 (0.04)
1284.3	20 (0.12)	1285	b _{1u}	1282.8	11.4 (0.09)
1165.2	5 (0.03)	1164		1174.4	0.27 (0.003)
1128.6	3 (0.02)		b _{2u}	1144.9	3.5 (0.03)
1124.7	4 (0.025)	1123	b _{1u}	1123.4	4.2 (0.04)
997.0	12 (0.07)	995	b _{2u}	996.2	3.6 (0.03)
956.0/ 953.6	14 (0.08)	957 ^e	b _{3u}	961.5	8.6 (0.07)
933.4	2 (0.012)	932		935.5	1.5 ((0.01)
895.3	135 (0.81)	905 ^e	b _{3u}	906.3	76.5 (0.63)
742.9/ 740.5	166 (1.00)	743 ^e	b _{3u}	747.3	80.0 (0.66)

^aLanghoff³⁷. Frequencies scaled by 0.958.^bThis work. Ar matrix at 12K.^cRelative intensities in parentheses.^dVodehnal and Stephan in crystalline phase²⁵.^eCyvin *et al* in crystalline phase⁴⁰.

Table 6. Vibrational analysis of cationic tetracene.

Experimental		Theory(B3LYP/4-31G) ^a		
ν (cm ⁻¹) ^b	Intensity ^b (km/mol) ^c	Irrep	ν (cm ⁻¹)	Intensity (km/mol) ^c
			3086.3	25.9 (0.04)
			1581.6	40.9 (0.06)
			1529.7	8.4 (0.01)
1543.3	55 (0.30)	b _{2u}	1518.8	197 (0.35)
1487.8/	27 (0.15)			
1486.3				
1478.2	60 (0.33)	b _{2u}	1478.5	201 (0.36)
1414.5	36 (0.20)	b _{1u}	1409.5	8 (0.01)
1409.7/	113 (0.62)	b _{2u}	1392.0	190 (0.34)
1406.3				
1401.5	13 (0.07)			
1358.6	182 (1.00)	b _{2u}	1349.5	556 (1.00)
1351.3/	96 (0.53)			
1348.9				
1332.1	11 (0.06)			
		b _{1u}	1288.6	24 (0.04)
		b _{2u}	1279.6	16 (0.03)
1178.8	96 (0.53)	b _{2u}	1189.0	139 (0.25)
		b _{2u}	1181.0	15 (0.03)
		b _{3u}	982.4	11 (0.02)
929.5	13 (0.05)	b _{3u}	934.3	55 (0.10)
766.5	16 (0.06)	b _{3u}	758.5	88 (0.15)

^aLanghoff³⁷. Frequencies scaled by 0.958.^bThis work. Ar matrix at 12K.^cRelative intensities in parentheses.

Table 7. Vibrational analysis of anionic tetracene.

Experimental ^a		Theory(B3LYP/4-31G) ^b		
ν (cm ⁻¹)	Relative Intensity	Mode ^c	ν (cm ⁻¹)	Intensity (km/mol) ^{d,e}
		R(CH)	3042.9	345 (0.43)
		R(CH)	3024.5	247 (0.31)
		R(CH)	3008.6	114 (0.14)
1530.2	0.22	R(CC)	1512.5	310 (0.39)
1473.8	0.15	R(CC)	1472.5	38 (0.05)
1385.0	0.59	R(CC)	1376.4	272 (0.34)
1339.9	1.00	R(CC)	1333.0	800 (1.00)
		R(CC)	1273.4	15 (0.02)
		R(CC)	1266.5	7 (0.01)
		β (CH)	1182.5	48 (0.06)
		R(CC)		
		β (CH)	1157.5	3 (0.004)
		β (CH)	1103.9	7 (0.009)
		β (CH)	1013.8	23 (0.03)
		R(CC)		
		ϵ (CH)	887.4	21 (0.03)
		ϵ (CH)	823.3	105 (0.13)
		β (CC)	736.6	37 (0.05)
		ϵ (CH)	716.4	72 (0.09)

^aThis work. Ar matrix at 12K.^bThis work. Experimental frequencies scaled by 0.958.^cNotation: R (stretching mode), β (in-plane bending), ϵ (out-of-plane) bending^dOnly theoretical frequencies with intensities greater than 2.0 km/mol reported.^eRelative intensities in parentheses.

As was the case for naphthalene, the relative intensities, with the exception of the CH stretch features, compared to the most intense band at $740.5/742.9\text{ cm}^{-1}$ are in good agreement with theoretical.

The experimental integrated intensities for tetracene cation listed in Table 6 indicate that if the intensities of the features at 1358.6 and $1351.3/1348.9\text{ cm}^{-1}$ were combined, the overall discrepancy between experimental and theoretical intensities would be about a factor of 2. Overall, the experimental relative intensities versus the combined intensities of features at 1358.6 and $1351.3/1348.9\text{ cm}^{-1}$ are in good agreement with theory.

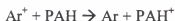
The intensities of the infrared absorption features assigned to tetracene anion listed in Table 7 were relatively small compared to tetracene cation. However, the agreement between experimental and theoretical values for both band positions and relative intensities is sufficient to verify the features as tetracene anion.

E. Discussion

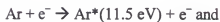
1. Ionization Mechanisms

In order to understand the increase in intensity of features corresponding to PAH anions when CCl_4 was removed from the isolant gas mixture, the mechanisms of ionization by the electron beam need to be considered. First, since there were approximately three orders of magnitude more Ar atoms than PAH molecules during deposition, the major ionization process for production of PAH cations was not simple electron bombardment of the PAH molecules. In fact, given the same electron gun parameters, the production of PAH cations increased when the pressure of the Ar isolant

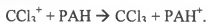
gas was increased. These results suggest that the production of PAH cations is primarily via charge transfer



and/or Penning ionization,



The next consideration is the addition of CCl_4 to the Ar isolant gas during deposition of the PAH molecules. CCl_4 was added as an ionization enhancer which operates via the charge transfer process,



CCl_3^+ , an electron impact product of CCl_4 , was proposed⁴¹ to be formed by the reaction,



Previous work on the ionization enhancement of PAH molecules by adding CCl_4 resulted in an approximately threefold increase in cation production⁴¹. The charge transfer process between PAH molecules and the CCl_4 electron impact products was corroborated by the presence of infrared peaks corresponding to CCl_3^+ , $\text{CCl}_3 \cdot \text{Cl}$ and CCl_3 at 1136.7, 926.6 and 898 cm^{-1} , respectively. The addition of CCl_4 also kept the potential on the matrix, caused by the deposition of positively charged species, lower than the kinetic energy of the PAH cations. The Cl atoms, acting as electron traps, maintained the charge balance.

Finally, the intensity of the anion features increased upon removal of CCl_4 from the Ar isolant gas because in addition to acting as electron traps, the Cl atoms also competed with neutral PAHs in the production of anions. The electron affinity (EA) of Cl atoms is 3.6 eV, while the EAs of pentacene and tetracene are 1.2 and 0.95 eV, respectively¹⁷. Therefore, the PAH anion features increased in intensity as the CCl_4 concentration was lowered in the Ar gas.

2. Fragmentation of PAHs

Ionization by an electron beam can also lead to fragmentation of hydrocarbons. Süzer and Andrews, while depositing C_2H_6 in an Ar matrix⁴², facilitated direct bombardment of the matrix surface with a low energy electron beam similar to that used in these studies. The direct bombardment produced fragments while no fragments were observed when the e-beam intersected the isolant/sample gas mixture prior to deposition. As was discussed in the previous section, since the electron beam intersected the samples in this work prior to deposition, the production of PAH cations is proposed to occur via charge transfer and Penning ionization. Both processes are “soft”, non-fragmenting ionization processes and no fragments were expected or observed.

The formation of anions by electron impact can also lead to the removal of hydrogen. Previous electron capture negative ion mass spectrometric studies⁴³ on PAHs determined that for species with EAs greater than 0.5 eV, the parent anions $(\text{PAH})^-$ were the primary constituent, while the hydrogen-abstracted ion $(\text{PAH-H})^-$ was the primary product for PAHs with EAs less than 0.5 eV. Therefore, the pentacene and tetracene anions observed in this work are proposed to be the parent ion.

3. Photolysis Process

The photolysis of matrix-isolated PAH cations with a medium pressure Hg lamp can lead to two possible competitive processes. Previous studies on naphthalene and anthracene cations have demonstrated both. In the naphthalene studies³⁶, the intensities of the cation bands increased upon annealing while the intensity of the anthracene cation²³ decreased. The two processes that can occur upon photolysis of the matrix are the production of cations through a two-color photoionization of the neutral species and the destruction of cations by electron/cation recombination.

If the lowest doublet state of the cation (D_0) is sufficiently close enough to the T_1 state of the neutral, a two step photoionization can produce cations. The equations⁴⁴ that describe the rate of change in the number of neutral molecules in the first excited singlet state (S_1) and in the first excited triplet state (T_1) are

$$N(S_1) = \tau(S_1)N(S_0)\omega(t) \quad (6)$$

and

$$N(T_1) = \tau(S_1)\tau(T_1)k_{isc}N(S_0)\omega(t) \quad (7)$$

where $\tau(S_1)$ and $\tau(T_1)$ are the lifetimes, k_{isc} is the intersystem $S_1 \rightarrow T_1$ crossing rate constant and $\omega(t)$ is the pumping rate which is constant for a cw source.

The formation of cations through two-color photoionization is proportional to the number of molecules in the S_1 or T_1 states. Therefore, approximating the population ratios between molecules that showed an increase in cation intensity (naphthalene) and molecules that showed a decrease in cation intensity (anthracene, tetracene and pentacene) may be useful in predicting photolysis behavior. Table 8 lists the numerical

values for various electronic state parameters of naphthalene, anthracene, tetracene and pentacene.

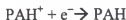
Table 8. Singlet state lifetimes (τ_S), triplet state lifetimes (τ_T), rates of intersystem crossing (k_{ISC}) and quantum yields for fluorescence (Φ_F) and intersystem crossing (Φ_{ISC}) for various PAHs.¹⁷

PAH	$\tau(S_1)$ (ns)	$\tau(T_1)$ (s)	k_{ISC} (10^6 s^{-1})	Φ_F	Φ_{ISC}
Naphthalene	~100	2.4	5	0.2	0.8
Anthracene	~10	.045	50	0.4	0.6
Tetracene	~10	.008	100	0.2	0.65
Pentacene				0.1	0.15

Examination of these parameters in the context of Equations (6) and (7) revealed that tetracene was expected to show the same behavior as anthracene upon photolysis. That is the two-color photoionization process would not be dominant and that the competing electron/cation recombination would cause a decrease in the intensity of spectroscopic features associated with the cation. In fact, the energy level of the excited singlet state for both tetracene and pentacene is low enough that the quantum efficiency of internal conversion to the singlet ground state, $S_1 \rightarrow S_0$, is sufficiently high. The quantum efficiencies for internal conversion, Φ_{IC} , are 0.75 and 0.20 for pentacene and tetracene²⁰, respectively. Fluorescence ($S_1 \rightarrow S_0$) and intersystem crossing ($S_1 \rightarrow T_1$) are normally the two possible relaxation mechanisms possible from the S_1 state and the sum of their quantum efficiencies is unity. The internal conversion efficiency of the tetracene and pentacene molecules is manifested in a less than unity sum for the fluorescence and intersystem crossing efficiencies.

The internal conversion efficiency for pentacene is relatively high and the pentacene neutral is expected to have a very small population density in the T_1 state. Therefore, two-color photoionization to the D_0 state of the cation molecule for pentacene neutral is expected to be much less efficient than anthracene or tetracene. Subsequently, the destruction of cations through electron/cation recombination is expected to be the dominant process during photolysis of the matrix-isolated pentacene cations and the corresponding features were expected to bleach.

A process that can compete with two-color photoionization production of cations during photolysis is the destruction of cations through electron/cation recombination. Electrons were released from matrix traps by photolysis and/or photodetached from molecular anions in the matrix and recombined with the PAH cation via the reaction,



The decrease in intensities of the pentacene and tetracene cation infrared features reflects the higher yield of the electron/cation recombination reaction over the two-color photoionization. Considering the relative population of the S_1 and T_1 states for pentacene and tetracene versus naphthalene and anthracene, the recombinative process is expected to dominate upon photolysis of the matrix with a medium pressure mercury lamp.

4. PAH Intensities and their Correlation with UIR Emission

In addition to ionization, dehydrogenation was considered a potential mechanism that a PAH would undergo as a result of absorbing the UV radiation in interstellar matter²⁰. The theory that partially dehydrogenated PAHs are the source of UIR emission is not without foundation. First, consider the correlation between the number of adjacent hydrogens around a neutral PAH and the frequency of the CH out-of-plane bending

modes. As depicted in Table 9, the frequencies of the modes decrease as the number of adjacent hydrogens increases. The most intense UIR emission in the CH out-of-plane bending region occurs at 11.3 μm , which is consistent with the compact (pericondensed) PAHs being partially dehydrogenated.

Table 9. Correlation of CH out-of-plane bending mode to number of adjacent hydrogens on the aromatic ring^a.

Number of Adjacent Hydrogen Atoms	ν (cm^{-1})	λ (μm)
1	900-860	11.11-11.63
2	860-800	11.63-12.50
3	810-750	12.35-13.33
4	770-735	12.99-13.61
5	770-730	12.99-13.70

^aAdapted from Conley⁴⁵.

Alternatively, the feature at 11.3 μm could also be explained by the presence of hydrogenated catacondensed PAHs such as tetracene and pentacene that have non-adjacent hydrogens. Duley and Jones proposed that the catacondensed, not pericondensed, structures were the most stable of the PAHs with the number of carbon atoms ranging from 15 to 27⁴⁶. Inspection of Tables 2 and 5 show that strong features for neutral pentacene and tetracene were observed at 902.5/900.2 (11.1 cm^{-1}) and 895.3 cm^{-1} (11.2 cm^{-1}), respectively.

Another point in favor of dehydrogenated PAHs as the source of UIR emission has been the ratio of intensities between the in-plane CC (6.2 μm) and the CH out-of-plane (11.3 μm) features. The ratio is about equal to or greater than 1.0 depending on the interstellar object of interest, while the neutral PAHs have an $I_{6.2 \mu\text{m}}/I_{11.3 \mu\text{m}}$ much less than

one. However, if the PAHs were dehydrogenated, the contribution to $I_{11.3 \text{ } \mu\text{m}}$ would decrease due to the loss of CH emitters and the $I_{6.2 \text{ } \mu\text{m}}/I_{11.3 \text{ } \mu\text{m}}$ ratio would increase and possibly correlate better with the UIR emissions.

Inspection of Table 10, which contains a compilation of data for PAH neutrals and cations⁴⁷ including this work, illustrates an alternative explanation for the $I_{6.2 \text{ } \mu\text{m}}/I_{11.3 \text{ } \mu\text{m}}$ ratio. Table 10 lists the individual and summed intensities for neutral and cationic PAHs in each region of interest for the UIR emission. The summed intensities of the PAH cations are approximately 55% less than the neutrals in the 11.3 μm region. In the 6.2 μm region the summed intensities of the cations was 4 times greater than the corresponding features for neutral. Overall, the ratio between the summed intensities for both regions ($I_{6.2 \text{ } \mu\text{m}}/I_{11.3 \text{ } \mu\text{m}}$) goes from 0.13 for neutrals to 1.5 for cations. The observed trend for the $I_{6.2 \text{ } \mu\text{m}}/I_{11.3 \text{ } \mu\text{m}}$ ratio going from neutrals to cations certainly makes the argument in favor of PAH cations as possible carriers of UIR emissions as strong as that for partially dehydrogenated PAHs.

5. PAH Ions in Interstellar Space

The identification and spectroscopic analysis of tetracene and pentacene anions raised the issue as to whether PAH anions should also be considered as a potential source of the UIR emissions. Evaluation of the theoretical IR spectra for neutral, cationic and anionic tetracene in Figure 27 predicts that the anions will have similar features to those of the cation. Is the environment of interstellar space conducive to the formation and continued existence of PAH anions and cations? The majority of stellar photon flux with $\lambda < 912 \text{ } \text{\AA}$ (13.6 eV) is absorbed by hydrogen atom ionization near circumstellar regions.

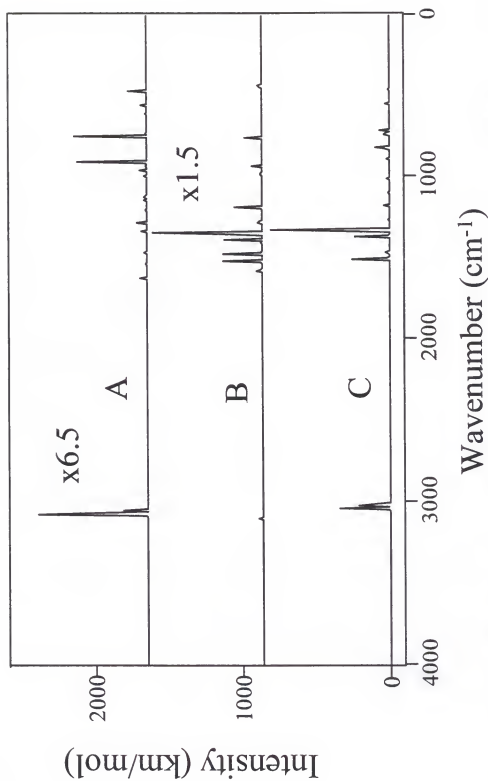


Figure 27. Theoretical spectra for tetracene calculated at the B3LYP/4-31G level of theory with Gaussian 94^{®39}. A. Neutral. B. Cation. C. Anion. The y-axis scale corresponds to the intensity (km/mol) of the anion spectrum.

Table 10. Integral intensities of IR absorption bands (Ar matrix at 12K) for several PAH neutral molecules and their cations in the UIR emission regions^a.

PAH	Intensity (Neutral/Cation) (km/mol)			
	11.3 μm 810-925 cm^{-1}	7.8 + 8.6 μm 1030-1400 cm^{-1}	6.2 μm 1525-1630 cm^{-1}	3.3 μm 3000-3100 cm^{-1}
Naphthalene ^b	1.4/	20/195	6/31	50/ ^c
Anthracene ^b	98/27	35/408	22/7	80/ ^c
Pyrene ^b	155/66	52/163	20/169	87/ ^c
Perylene ^b	100/97	52/497	17/149	60/ ^c
Coronene ^b	135/71	57/24	14/	54/ ^c
Tetracene	135/13	68/385	3/55	69/ ^c
Sum	624.4/274	284/1672	82/411	400/

^aTable adapted from Szczepanski and Vala⁴⁸

^bSzczepanski and Vala⁴⁷.

^cExperimental values not observed possibly due to overlap with neutral. Theory predicts very low intensities³⁷.

Tetracene and pentacene have ionization potentials of 7.04 and 6.74 eV, respectively¹⁸.

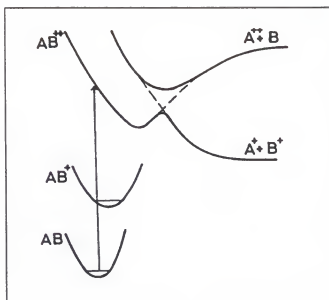
Therefore, if the two neutral molecules were in interstellar space, a reasonable hypothesis would be that the cations would be formed.

The stability of PAH⁺ in the interstellar environment is the next consideration.

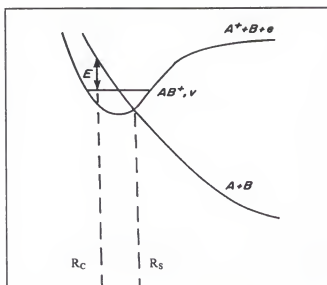
There are four possible mechanisms for removal of the PAH⁺:



Observations during deposition and photolysis of matrix-isolated pentacene and tetracene cation did not indicate fragmentation either by dissociative recombination, Equation (9), or two-photon photodissociation, Equation (11). Examination of the potential energy curves illustrating both effects in Figure 28 leads to the following conclusions.



A



B

Figure 28. Potential energy curves depicting the dissociation of PAH cations. (A) Neutral, singly ionized and doubly ionized molecule depicting two photon dissociation. Adapted from Leach¹⁸. (B) Schematic representing the arrangement of potential energy curves necessary for dissociative recombination. E is the kinetic energy of the electron in the reaction $\text{PAH}^+ + e^- \rightarrow \text{PAH}(\text{neutral fragments})$ Adapted from Duley and Williams⁴⁹.

In order for a cation to undergo two-photon dissociation in an interstellar environment, the ionization potential of the cation would probably need to be less than ~ 13.6 eV. The radiation flux in interstellar medium decreases considerably at energies higher than 13.6 eV (~ 1000 Å) as illustrated in Figure 29. There is also the possibility that the geometry of the singly charged cation was sufficiently different from the doubly charged cation that a vertical transition to the dissociative potential energy curve of the molecule⁴⁹ is possible.

Since the IP's of the cations are 15.10 and 12.86 eV, respectively¹⁸, the only pathway to dissociation of these molecules by the medium pressure mercury lamp was via a direct vertical transition to the dissociative potential surface. No new features were observed in the infrared or electronic spectra after photolysis of the sample matrices that contained cations, therefore photodissociation by this mechanism did not occur. Tetracene in interstellar space would need to undergo a direct vertical transition to the dissociative potential surface, from either the neutral or cation state, in order to dissociate since the IP of the cation is greater than 13.6 eV. The pentacene molecule, however, could fragment via dissociation of the doubly charged species or by a direct vertical transition to the fragmentation potential surface since the cation IP is less than 13.6 eV.

Another pathway for the elimination of a PAH cation in interstellar space is via reaction with an electron. Interaction of the PAH^+ with an electron can have two possible outcomes indicated in Equations (8) and (9). Electron/cation recombination is very likely considering the observation of the process upon photolysis of the sample matrices in this study. However, in interstellar space, molecular recombination with an electron is not more likely to occur than photon ionization so that at the very least both neutral and

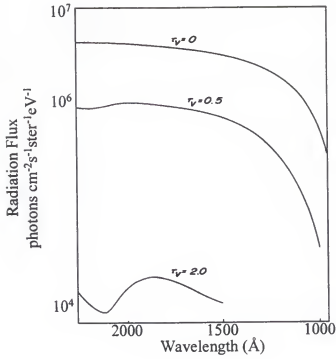


Figure 29. Photon flux in interstellar medium ($\tau_v=0$), diffuse cloud ($\tau_v=0.5$) and denser cloud ($\tau_v=2.0$). Adapted from Duley and Williams⁴⁹.

cationic PAHs could exist. Assuming, of course, that two-photon dissociation did not contribute significantly to cation fragmentation. Dissociative recombination of the PAH cation and an electron, as illustrated in Figure 28B, would require that the potential surface of the neutral fragment products lie very close to the potential surface of the cation. Again, no fragments attributable to dissociative recombination were observed as a result of producing tetracene and pentacene cations in an electron beam.

The formation and stability of PAH anions in interstellar space needs to be considered next. The generation of anions in interstellar matter is possible via radiative attachment,



Compared to radiative recombination discussed previously, the rate coefficient of radiative attachment is much smaller. In contrast, photodetachment, which is the inverse process,



is an efficient one in interstellar matter⁴⁹. Figure 30 represents an approximate cross section for the electron photodetachment from H^- as a function of wavelength. The wavelength range of photons that can detach the electron is very large and the same is expected for other anionic systems due to the low interaction energy and large electron-neutral separation indicative of anionic molecules⁴⁹.

In the current study, photodissociation of tetracene and pentacene anions was observed when the sample matrices were photolyzed with a medium pressure Hg lamp. The anion features decreased upon photolysis according to the reaction in Equation 13. Based on the photodetachment cross section in Figure 30 and the laboratory

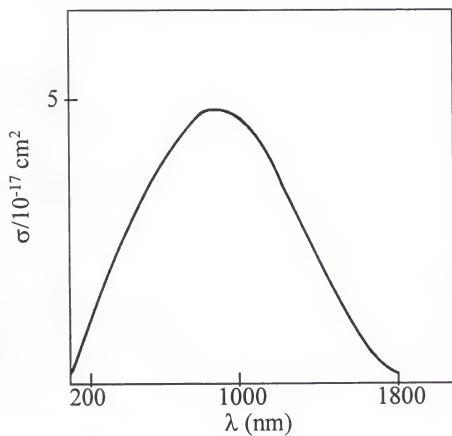


Figure 30. Approximate cross section for $\text{H}^+ + h\nu \rightarrow \text{H} + \text{e}^-$ as a function of wavelength. Adapted from Duley and Williams⁴⁹.

investigations, the equilibrium between radiative attachment and photodetachment in interstellar objects would probably favor neutral PAHs. Anions would be unlikely to exist in interstellar matter at quantities sufficient to account for the UIR emission. Perhaps anions could avoid photodetachment in denser regions, but then the probability of interaction with other molecules would increase and anion destruction via associative detachment and/or mutual neutralization would occur.

III. INFRARED INVESTIGATIONS OF CARBON CLUSTERS

A. Carbon Clusters and their Astrophysical Connection

The concept of carbon clusters as important constituents in astrophysical science is definitely not a new one. Following the laboratory assignment of C_3 by Herzberg in 1942⁵⁰, Douglas assigned an emission⁵¹ and an absorption feature⁵² at 4050 Å to C_3 ⁵³. The sources were comets and, unlike interstellar matter, had the necessary UV flux for detection of the 4050 Å feature. Thermodynamic calculations in the mid-1960's predicted the existence of carbon clusters in the atmospheres of carbon stars⁵⁴ but the lack of dipole moment in linear C_n prevented their detection by pure rotational microwave spectroscopy. Then the identification of the long chain carbon molecules, $HC_{2n+1}N$ ($n=1-5$)^{55,56,57,58,59} in various interstellar and circumstellar regions prompted a series of experiments involving the vaporization of graphite that led to the discovery of the fullerenes⁶⁰. Eventually, by adding hydrogen and nitrogen to the condensation process, the same long chain carbon molecules, cyanopolyynes, were produced⁶¹.

The discovery added a new perspective to the idea of how molecules in interstellar matter were formed. Most of the identified species in interstellar matter were predicted to form by sequences of bimolecular ion-molecule reactions and on the surface of interstellar grains⁴⁹. Since the long chain polyynes and larger carbon clusters (C_{60} , C_{70} e.g.) were formed under high temperature processes, the proposal was that the same type of high temperature reactions were also responsible for carbonaceous grains and that the

interstellar grains originated in circumstellar regions⁶¹. Finally, in 1988 and 1989, the carbon chains C_3 and C_5 were identified in the IR studies of the circumstellar region, IRC+10216^{62,63}. Long chain carbon molecules have also been proposed to be the source of the diffuse interstellar bands (DIBs) and as the starting material for PAHs^{61, 64}.

Mass spectrometric studies^{65,66,67} of the carbon chains, C_n ($n=1-5$), generated in carbon vapor date back to the early 1950's. In 1988 Weltner and Van Zee reviewed carbon clusters thoroughly. The knowledge of carbon clusters (C_n), as the article so eloquently stated, was "almost a monotonically decreasing function of n "⁶⁸. Due to the large number of features in the infrared spectrum of carbon vapor, the sorting process had proceeded slowly. At the time, isotopic studies had verified C_3 ⁶⁹ and C_5 ⁷⁰ infrared absorption (asymmetric stretch mode) features at 2038 and 2164 cm^{-1} in Ar at 12K, respectively. Subsequent infrared matrix isolation, gas phase and theoretical studies have identified features corresponding to C_4 ^{71,72} and C_6 ^{73,74,75}. Partial isotopic investigations have verified features corresponding to C_7 ⁷⁶ and C_9 ⁷⁷.

The reactivity of C_n carbon chains with other molecules to produce species that may be common in interstellar space has also been investigated. Table 11 gives a list of products produced when various reactants combine with carbon clusters formed from vaporized graphite.

Table 11. Carbon cluster reaction products⁶¹.

Reactants	Main Products
H_2	$C_6H_2-C_{22}H_2$
N_2	$C_8N_2-C_{22}N_2$
CH_3CN	HC_7N-HC_9N
NH_3	HC_7N-HC_9N
H_2O	$C_8H_2-C_{20}H_2$

Initial gas chromatographic (GC) studies of the reaction of atomic carbon with water in conjunction with very detailed theoretical calculations concluded that $C(^1D)$ atoms and not ground state $C(^3P)$ atoms reacted with H_2O to produce CO , H_2 and H_2CO ⁷⁸. These results were verified by matrix-isolation results by Ortman *et al*⁷⁹ where no products for the reaction of atomic carbon with water were observed. Assuming that the ground state of atomic carbon is the form deposited at cryogenic temperatures on a matrix, the observation was expected. Whether the atomic carbon complexed with water was not confirmed. Either no complex was formed or the H_2O vibrational modes of $C\cdot H_2O$ were not observable in the IR spectrum. No C_2/H_2O reaction products were observed, but the results were substantially more interesting regarding the reaction of C_3 with H_2O .

Infrared matrix-isolation spectroscopic studies of laser ablated carbon vapor deposited with Ar isolant gas revealed a new feature at 2052 cm^{-1} when H_2O was added to the gas mixture. The peak was assigned to the $C_3\cdot H_2O$ complex and subsequent photolysis of the matrix revealed features corresponding to C_3O and propynal (HC_3OH)⁷⁹, both of which have been identified in the molecular cloud, TMC-1⁸⁰. Additional intermediate features were also observed after photolysis at $\lambda > 400\text{ nm}$. These features decreased upon photolysis at $280\text{ nm} < \lambda < 360\text{ nm}$ while features corresponding to propynal increased. Subsequent theoretical and experimental isotopic studies have verified the assignment of the 2052 cm^{-1} feature to $C_3\cdot H_2O$ and have further clarified transition states and the identity of the intermediate features as due to transoid 3-hydroxypropadienylidene (t-HPD)^{81,82}.

In addition, matrix-isolation of the $C_3 \cdot H_2O$ system allowed identification of the very short-lived cisoid rotamer of t-HPD via concurrent infrared scanning of the matrix while it was being photolysed.⁸² Subsequent matrix-isolation studies focusing on the longer C_n clusters identified new features at 2014 and 1959 cm^{-1} upon annealing the matrix, which were tentatively assigned to $C_9 \cdot H_2O$ and $C_6 \cdot H_2O$, respectively⁸³. Theoretical and experimental investigations of the proposed carbon chain water clusters could provide additional information regarding the reactivity of the clusters under conditions similar to that on grains in interstellar matter.

Recent experimental studies have shown an interesting correlation between carbon chain anions and some of the diffuse interstellar bands (DIBs)⁸⁴. Subsequent matrix-isolation infrared spectroscopic work investigating the asymmetric stretch modes have tentatively assigned features corresponding to the anionic clusters C_n^- ($n=3, 5, 6, 7$ and 9)⁸⁵. Although experimental work has verified that these clusters are photosensitive and would undergo photodetachment under interstellar conditions, theoretical calculations predict that anion-neutral clustering is very exothermic. The small anionic clusters could play an important role in the formation of larger anionic clusters, which early studies indicate are more photostable under UV irradiation^{84,86}.

In this dissertation attention was focused on the smallest polyatomic carbon anion C_3^- . Of specific interest was the asymmetric stretch mode of C_3^- tentatively assigned to a band at 1721.8 cm^{-1} ⁸⁵. Three criteria were used for the assignment: (1) Electron photodetachment studies had found a threshold energy of 1.99 eV for C_3^- in the gas phase. The matrix-isolation studies determined that the band was found to decrease in intensity starting at an energy of 2.19 eV. (2) The annealing behavior of the band

assigned to C_3^- was very similar to that of C_3 . and (3) Theoretical studies had calculated an asymmetric stretch frequency of 1772 cm^{-1} (unscaled) for C_3^- at the B3LYP/6-31G* level of theory. Raghavachari proposed that the anion had a linear structure with a $^2\Pi_g$ electronic ground state⁸⁷. Matrix-isolation infrared isotopic studies for the neutral C_3 molecule were able to verify the assignment of the asymmetric stretching mode⁶⁹ at 2038 cm^{-1} and determine a bent configuration⁸⁸ of the molecule in an Ar matrix at an angle of 162° . A similar study of the anion was undertaken in order to verify the asymmetric stretch mode assignment and the ground state geometry of the C_3^- carbon cluster.

B. Experimental

Figure 31 is a diagram of the experimental setup for the generation of carbon clusters in an Ar matrix. Graphite vaporized by a pulsed laser (Nd/YAG, DCR-11, Spectra Physics) produced the carbon clusters. For ^{12}C -only species, a graphite rod (Alfa, 99.9995% pure) was laser ablated. In order to generate $^{12}\text{C}:^{13}\text{C}$ isotopic species a pressed powder consisting of ^{12}C from the graphite rod samples and ^{13}C (Isotec, 98.4% atom %) was vaporized. Enhancement of $C_n\cdot\text{H}_2\text{O}$ clusters was accomplished by adding $\sim 0.1\%$ H_2O to the Ar isolant gas. At any time, very small amounts of H_2O were present due to the combined effect of the staying power of H_2O on the apparatus walls and the humidity associated with our geographical location.

Figure 32 is a schematic of the experimental setup used for the preparation of C_n ions. Small linear carbon clusters C_n ($n < 10$) have been generated by low energy laser ablation of a graphite rod. In order to produce the negative ions of these linear species, an electron beam and/or plasma are added as an electron source. For this experiment a pulsed (10 Hz) fundamental (1064 nm) Nd-YAG laser beam was dispersed from the

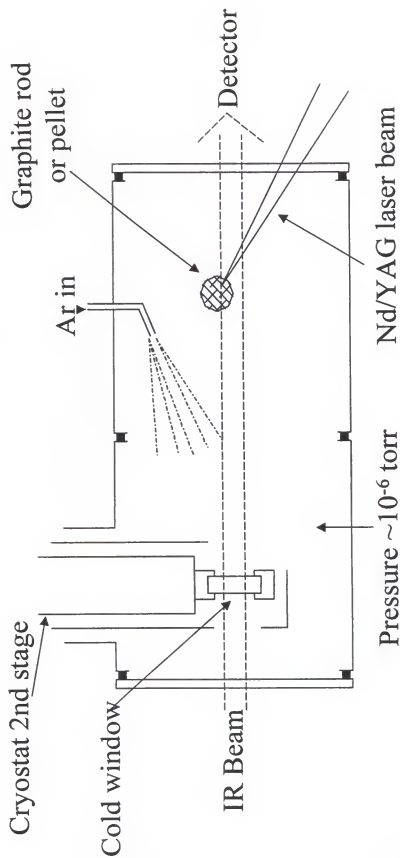


Figure 31. Experimental setup for preparation of carbon clusters in Ar matrix at 12 K.

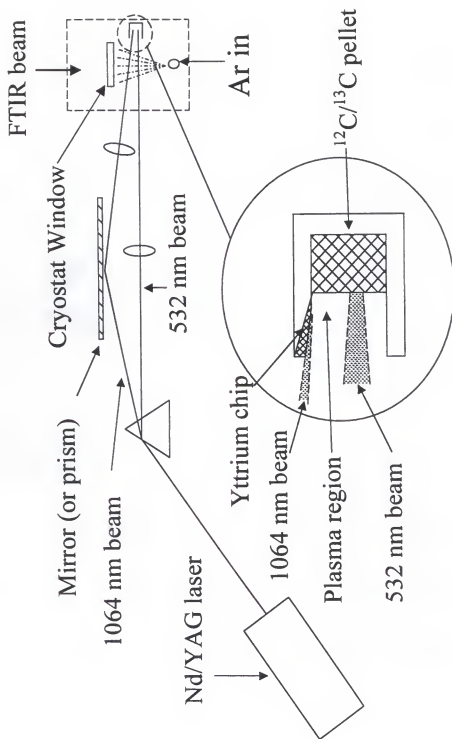


Figure 32. Schematic for generation of C_n^- carbon clusters.

second harmonic (532 nm) beam. The 532 nm beam was focused on the sample holder containing a pressed powder mixture of ^{12}C and ^{13}C while a portion of the fundamental beam was focussed on the yttrium chip located in the sample holder. The 1064 nm beam generated a plasma near the surface of the pressed powder mixture and provided a source of electrons for the carbon clusters.

The $^{12/13}\text{C}$ sample holder, 7 mm in diameter, was 2 cm from the cryostat window and 3.5 cm from the window axis and mounted on the thermal shield of the cryostat in order to reduce the level of impurities such as CO and CO_2 . The anionic clusters were extracted from the vaporization region by a 30-60 V O-ring electrode, mixed with matrix gas (Ar) and trapped on the BaF_2 cryostat window (12K) cooled by a closed-cycle helium cryostat. The average current collected by the O-ring during matrix deposition was 10-30 μA . A MIDAC FT-IR spectrometer with 0.7 cm^{-1} resolution recorded the absorption spectra.

C. $\text{C}_n\cdot\text{H}_2\text{O}$ Complexes

1. Infrared Spectra

Several techniques were utilized in order to conclusively assign the features tentatively attributed to $\text{C}_9\cdot\text{H}_2\text{O}$ and $\text{C}_6\cdot\text{H}_2\text{O}$. First, the behavior of the features upon annealing of the matrix was noted. Typical water complex bands grow upon annealing of the matrix, however, more proof is necessary for a definite assignment. One observation that can be useful is the ratio of intensities, $A(\text{C}_n\cdot\text{H}_2\text{O}):A(\text{C}_n)$, as the concentration of H_2O is increased. Another method for identification of complexes involves isotopic

substitution. If the isotopic shift of the complex band is in accordance with the isotopic shift of the parent band, the observation further verifies the assignment of the feature as the water complex. For $C_3 \cdot H_2O$, each $^{12,13}C$ isotopomer was identified⁸² and assigned in accordance with theoretical calculations.

In addition to the features tentatively assigned to $C_9 \cdot H_2O$ and $C_6 \cdot H_2O$ ⁸³, a feature at 1550.4 cm^{-1} was also observed and tentatively assigned to $C_4 \cdot H_2O$. Figure 33 shows the growth of the 2014.4 and 1959.4 cm^{-1} features upon annealing of the matrix, which have been assigned to $C_9 \cdot H_2O$ and $C_6 \cdot H_2O$, respectively. The growth of these peaks also coincided with the growth of the doublet assigned to C_9 at $\sim 2000\text{ cm}^{-1}$ and the depletion of $C_3 \cdot H_2O$, C_3 and C_6 . Figure 34 shows the spectra for the same runs as depicted in Figure 33 but in a different spectral region and absorbance range. Figure 34B depicts the growth of the feature at 1550.4 cm^{-1} assigned to the $C_4 \cdot H_2O$ cluster. The depletion of the feature at 1543.6 cm^{-1} corresponded to linear C_4 whose assignment has been verified by isotopic studies⁷¹.

Figure 35 shows that as the concentration of H_2O in the matrix was increased, the ratio of $C_9 \cdot H_2O:C_9$ and $C_6 \cdot H_2O:C_6$ also increased. The concentration of H_2O in the matrix increased going from the bottom to the top spectrum. The increase in intensity of the features, which coincided with the increase in H_2O concentration, supports the premise that the band is due to a water complex.

To aid in the assignment of the $C_9 \cdot H_2O$ and $C_6 \cdot H_2O$ water complexes, H_2O ¹⁸ was added to the Ar isolant gas. However, there were no observed shifts in the frequencies of the water complex bands. $^{12,13}C$ isotopic studies did manifest a shift in the frequency of one of the tentatively assigned water complex bands. Figure 36 shows the isotopic shifts

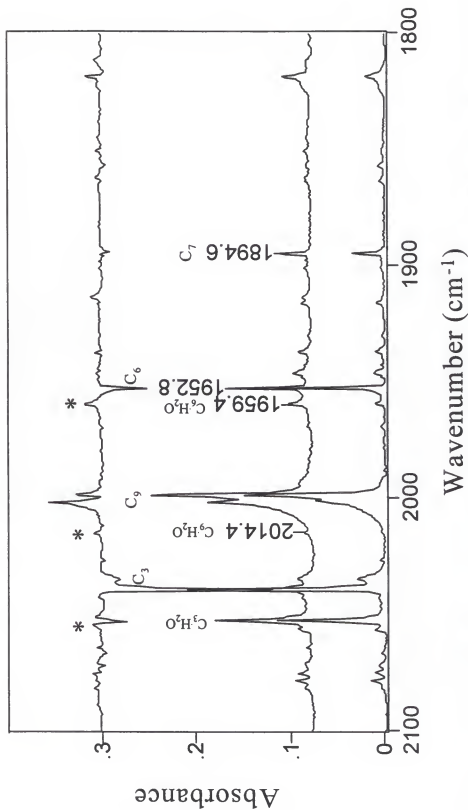


Figure 33. Infrared absorption spectra depicting the growth of $\text{C}_n\cdot\text{H}_2\text{O}$ features upon annealing of the matrix. Sample prepared with carbon vapor in Ar isolant gas with 0.1% H_2O at 12K. Bottom spectrum is before annealing. Middle spectrum is after annealing to $\sim 32\text{K}$. Top spectrum is the subtraction (after annealing minus before annealing) spectrum depicting the growth of $\text{C}_3\cdot\text{H}_2\text{O}$ and $\text{C}_6\cdot\text{H}_2\text{O}$ clusters and the depletion of $\text{C}_3\cdot\text{H}_2\text{O}$.

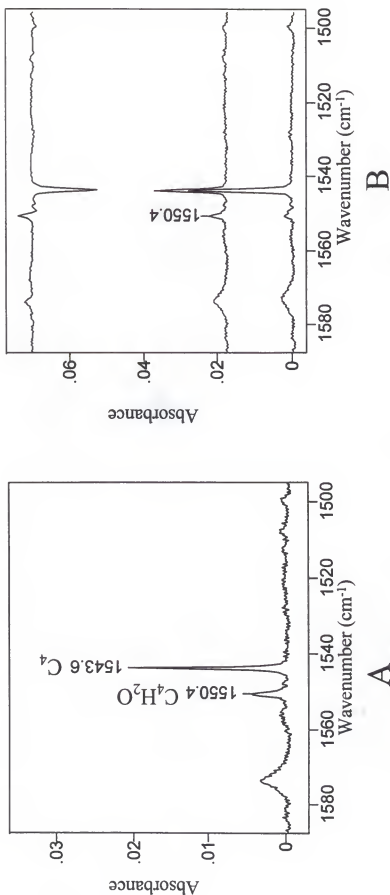


Figure 34. Infrared absorption spectra of $\text{C}_4\cdot\text{H}_2\text{O}$. (A) Infrared spectrum of C_4 and corresponding $\text{C}_4\cdot\text{H}_2\text{O}$ feature produced in carbon vapor deposited with Ar isolant gas with 0.1% H_2O and after annealing to 32 K. (B) Spectra depict the growth of $\text{C}_4\cdot\text{H}_2\text{O}$ after annealing. Bottom spectrum collected before annealing at 12 K. Middle spectrum is the spectrum depicted in (A) collected after annealing. Top spectrum is the subtraction (after annealing minus before annealing) depicting the growth of $\text{C}_4\cdot\text{H}_2\text{O}$ and the corresponding decrease in C_4 .

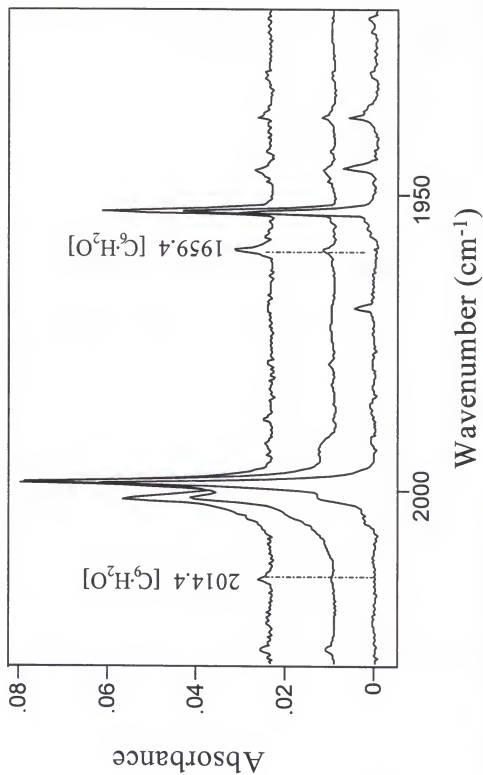


Figure 35. Infrared spectra depicting the increase in intensity of C₉•H₂O and C₆•H₂O features versus C₉ and C₆ as the concentration of H₂O in the Ar isolant gas was increased.

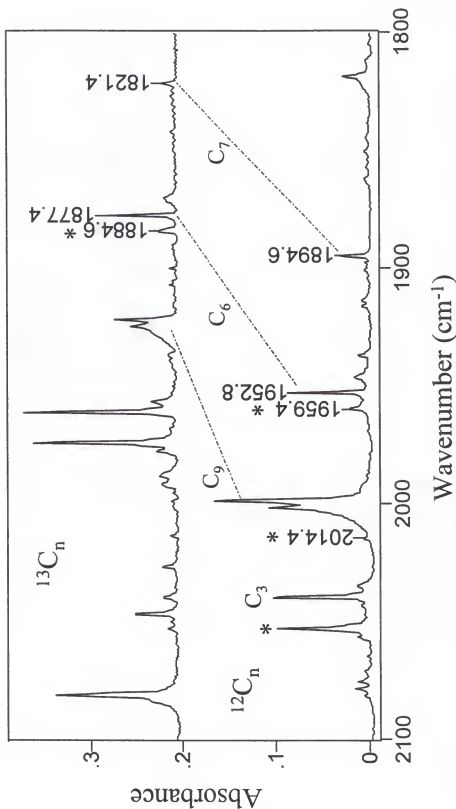


Figure 36. Infrared absorbance spectra of an all ¹³C deposit and an all ¹²C deposit. Both spectra were collected after annealing the matrix. The isotopic shift of the ¹³C₆H₂O feature can be seen clearly while the ¹³C₉H₂O feature is overlapped by another broad peak. The concentration of C₄ produced in the ¹³C deposit was not sufficient to observe ¹³C₄H₂O.

(^{12}C and ^{13}C) for C_9 and C_6 . Due to the low intensity of the $\text{C}_9\cdot\text{H}_2\text{O}$ cluster, the ^{13}C feature was not positively verifiable due to the presence of another band. The isotopic shift of the feature assigned to $\text{C}_6\cdot\text{H}_2\text{O}$ was very clear. Assignments of additional $^{12,13}\text{C}$ isotopomers for $\text{C}_6\cdot\text{H}_2\text{O}$ along with corresponding theoretical calculations are presented in a later section. A feature corresponding to $^{13}\text{C}_4$ was not detectable after laser vaporization of the $^{12}\text{C}:^{13}\text{C}$ pellet. The vaporization of the pellet required the laser power to be sufficiently less than when vaporizing the graphite rod. The intensity of the C_4 feature observed under such low power conditions is normally very small.

For the $\text{C}_3\cdot\text{H}_2\text{O}$ complex, photolysis of the sample matrix produced some very interesting results that were discussed in the first section of this chapter. Figures 37 and 38 present the behavior of the three water complexes, $\text{C}_9\cdot\text{H}_2\text{O}$, $\text{C}_6\cdot\text{H}_2\text{O}$ and $\text{C}_4\cdot\text{H}_2\text{O}$, after photolysis with a medium pressure mercury lamp. The $\text{C}_9\cdot\text{H}_2\text{O}$ feature completely disappeared after photolysis using a glass filter. The $\text{C}_6\cdot\text{H}_2\text{O}$ and $\text{C}_4\cdot\text{H}_2\text{O}$ features decreased only after photolysis for an hour with no filter. No new infrared features corresponding to photolysis products were observed.

2. Theoretical Results

Table 12 is a comparison of the experimental and theoretical shifts between the linear clusters, C_n , and the corresponding H_2O water cluster. The HF/6-31G* level of theory and basis set were utilized since this was the highest level that would converge on a geometry for the $\text{C}_9\cdot\text{H}_2\text{O}$ molecule given the computational capabilities. The geometries for the $\text{C}_n\cdot\text{H}_2\text{O}$ clusters were optimized by constraining the carbon chain to remain linear and allowing the H_2O molecule complete freedom to optimize. Each of the

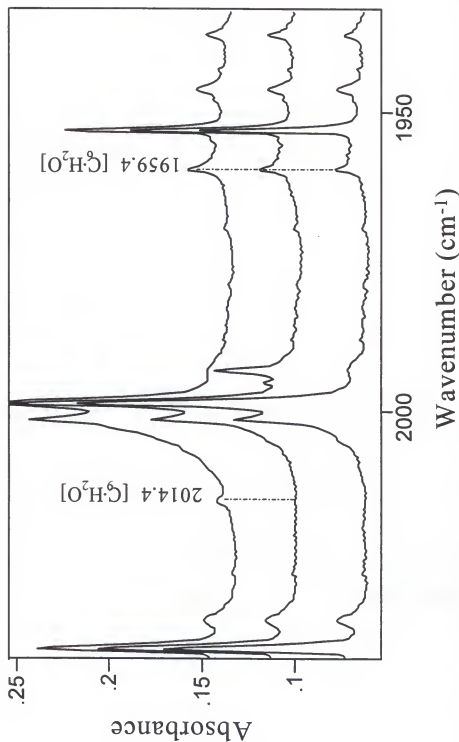


Figure 37. Infrared spectra depicting the effect of photolysis by a medium pressure Hg lamp on the $\text{C}_6\text{H}_2\text{O}$ and $\text{C}_6\text{H}_2\text{O}$ features. The top spectrum corresponds to the original sample matrix at 12K produced by laser vaporization of graphite and depositing with Ar isolant gas mixed with 0.1% H_2O . The middle spectrum was collected after photolysis of this sample matrix for one hour using a glass filter. The bottom spectrum was collected after photolysis for one hour with no filter.

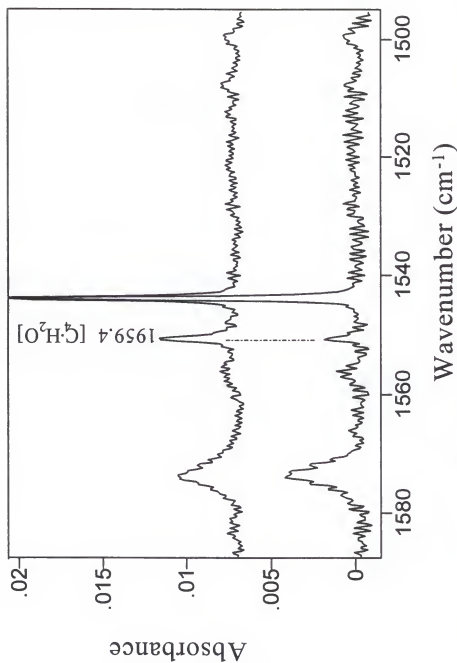


Figure 38. Infrared spectra depicting the effect photolysis by a medium pressure Hg lamp had on the C₄H₂O features. The top spectrum corresponds to the original sample matrix at 12K produced by laser vaporization of graphite and depositing with Ar isolant gas mixed with 0.1% H₂O. . The bottom spectrum was collected after photolysis of this sample matrix for one hour using no filter.

Table 12. Comparison of experimental and theoretical shifts ($\Delta\nu$) between the neutral cluster, C_n , and the water cluster, $C_n \cdot H_2O$.

n	C_n ν (cm^{-1})		$C_n \cdot H_2O$ ν (cm^{-1})		$\Delta\nu$ (cm^{-1})	
	Exp (Ar matrix)	Theory ^a (HF/6-31G*)	Exp (Ar matrix)	Theory ^b (HF/6-31G*)	Exp (Ar matrix)	Theory (HF/6-31G*)
3	2038.9 ^c	2057.8	2052.3 ^g	2062.5	13.4	4.7
4	1543.6 ^d	1548.6	1550.4	1556.4 ^h	5.0	7.8
6	1952.8 ^e	1949.1	1959.4	1949.1	6.6	0.0
9	1998.0 ^f	1854.7	2014.4	1870.2	16.4	15.5

^aMartin and Taylor⁸⁹. Frequencies are scaled by a factor of 0.89.^bThis work. Frequencies are scaled by a factor of 0.89.^cAssigned by Weltner *et al.*⁶⁹.^dAssigned by Shen and Graham⁷¹.^eAssigned by Vala *et al.*⁷³.^fPartial isotopic studies assigned by Graham *et al.*⁷⁶.^gAssigned by Szczepanski *et al.*⁸².^hThe C_4H_2O cluster would only converge at a singlet state, contrary to the expected triplet state.

optimized geometries consisted of the H₂O molecule bridge occurring from a hydrogen to a terminal carbon.

The discrepancy between the experimental and theoretical shifts for C₃•H₂O versus the C₃ molecule could be due to the fact that the actual geometry of the C₃ molecule is bent in an Ar matrix. The theoretical results for C₄•H₂O were interesting. In addition to the fact that theory would not converge on the expected triplet state H₂O complex for C₄, the experimental shift is not in bad agreement with theory. Higher level calculations at the MP2/6-31G* also would not converge on a triplet state for C₄•H₂O, but did converge on a singlet state. Spin contamination could be causing problems in calculating the triplet state C₄•H₂O complex.

At both the HF/6-31G* and MP2/6-31G* levels of theory, the triplet state C₆•H₂O molecule was predicted to have no shift in frequency for the asymmetric stretch mode versus linear C₆. The experimental frequency shift for the C₉•H₂O molecule was in good agreement with the theoretical shift, but the actual scaled frequencies have the largest discrepancy with regard to experimental values.

3. Isotopomer Assignments for C₆•H₂O

The theoretical frequencies for the isotopomers of C₆•H₂O were calculated at the MP2/6-31G* level of theory using Gaussian 94®³⁹. A linear scaling factor according to the protocol defined by Martin *et al* in the assignments of C₆, C₇ and C₉ was utilized. Essentially the theoretical frequencies were scaled to be equivalent to the experimental values for the ¹²C and ¹³C isotopomers and the remaining bands were scaled to a best fit line between the two scaling factors.

Assignment of the $C_6 \cdot H_2O$ isotopomers over the complete range from ^{12}C at 1959.4 cm^{-1} to ^{13}C at 1884.6 cm^{-1} was hampered by overlap with the C_9 “doublet” feature. Both features increased in intensity upon annealing and unlike the $C_3 \cdot H_2O$ and $C_9 \cdot H_2O$ features that bleach under photolysis by a medium pressure Hg lamp, the $C_6 \cdot H_2O$ feature manifested only a small decrease in intensity. The C_9 “doublet” feature at 2000 cm^{-1} also decreased slightly upon photolysis, therefore, differentiating between the $C_6 \cdot H_2O$ and the C_9 doublet isotopomers over the wavenumber range 1959 to 1921 cm^{-1} was not feasible.

Over the range 1920 to 1884.6 cm^{-1} , the $C_6 \cdot H_2O$ isotopomers were assigned according to the observation of positive features in the subtraction spectrum shown in Figure 39 (after annealing – before annealing) and the results are presented in Tables 13-15. Linear C_7 was also present in this range but the identification of the isotopomers in this region have been previously reported⁷⁶. The letter assignments correspond to the linear C_6 isotopomers listed in Tables 13-15. The starred letter assignments are the water complex isotopomers of the corresponding linear C_6 isotopomers. Each completely symmetrical C_6 isotopomer has one possible water complex configuration, while the non-symmetrical isotopomers have two possible water complex configurations (i.e. an H_2O could be at either end of the carbon chain). The remaining theoretical isotopomer bands that are predicted to lie outside the region 1920 - 1884.6 cm^{-1} are listed in Tables 16-18.

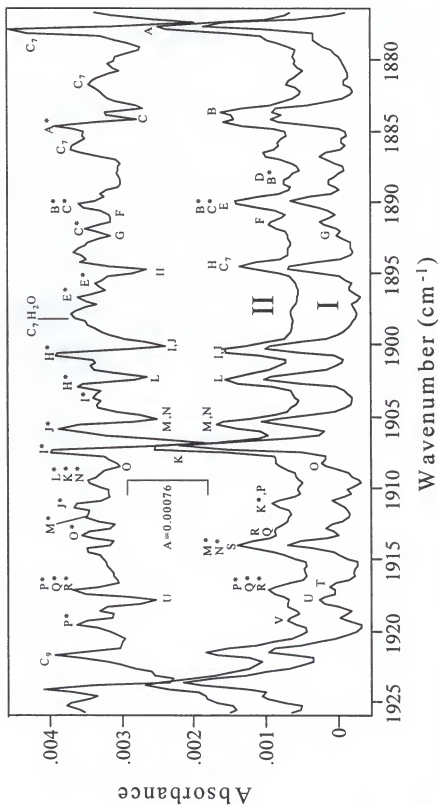


Figure 39. Infrared spectra for identification of C₆H₂O isotopomers. Spectrum I collected after deposit at 12K of laser ablated ^{12,13}C pellet with Ar/0.1% H₂O. Spectrum II collected after annealing the same matrix to 32 K. Top spectrum is the subtraction spectrum (II minus I). The y-axis scale applies to (I) and (II) while the scale A=0.00076 applies to the top spectrum.

Table 13. Assignment of $C_6 \cdot H_2O$ isotopomers.

Isotopomer	C_6 Molecule			$C_6 \cdot H_2O$ Molecule			
	Isotopic Shifts			Isotopic Shifts			
	ν (Obs) ^a (cm ⁻¹)	Obs ^a (cm ⁻¹)	Obs ^b (cm ⁻¹)	MP2/ 6-31G ^{*c}	ν (Obs) ^a (cm ⁻¹)	Obs ^a (cm ⁻¹)	MP2/ 6-31G ^{*a}
13-13-13-13-13 (A)	1877.4	75.4	75.3	75.3	1884.6	74.8	74.8
12-13-13-13-13-13 (B)	1883.4	69.4	69.4	70.2	1889.3 1890.2	70.3 69.2	70.8 68.1
13-13-12-13-13-13 (C)	1884.1	68.7	68.7	68.4	1890.2 1891.8	69.2 67.6	68.3 67.4
12-13-13-13-13-12 (D)	1888.6	64.2	64.2	65.2			64.3
13-13-13-12-13-12 (E)	1889.9	62.9	63.0	64.4	1895.7 1896.6	63.7 62.8	64.2 62.7
13-13-12-13-13-12 (F)	1891.3	61.5	61.3	62.5			63.6 59.9

^aThis work. Observed values are in Ar matrix at 12K.^bRef (73).^cRef (75).

Table 14. Assignment of C_6H_2O isotopomers (cont.).

Isotopomer	C_6 Molecule			C_6H_2O Molecule		
	Isotopic Shifts			Isotopic Shifts		
	ν (Obs) ^a (cm ⁻¹)	Obs ^a (cm ⁻¹)	MP2/ 6-31G ^{*c}	ν (Obs) ^a (cm ⁻¹)	Obs ^a (cm ⁻¹)	MP2/ 6-31G ^{*a}
13-13-12-12-13-13 (G)	1892.3	60.5	59.0			58.9
12-13-13-12-13-12 (H)	1894.7	58.1	58.7	1900.6 1902.9	58.8 56.5	58.4 57.0
13-13-12-12-13-12 (I)	1900.2	53.5	54.1	1903.6 1907.4	55.8 52.0	55.1 52.6
13-12-13-13-13-13 (J)	1900.2	52.6	51.3	1905.8 1911.3	53.6 48.1	53.2 47.8
13-13-13-13-12-12 (K)	1906.9	50.5	48.4	1909.6 1918.5	49.8 40.9	48.9 41.0
12-13-12-12-13-12 (L)	1902.6	50.2	49.6	1909.6	49.8	49.2

^aThis work. Observed values are in Ar matrix at 12K.^bRef (73).^cRef (75).

Table 15. Assignment of C₆H₂O isotopomers (cont.).

Isotopomer	C ₆ Molecule				C ₆ H ₂ O Molecule			
	ν (Obs) ^a (cm ⁻¹)		Isotopic Shifts		ν (Obs) ^a (cm ⁻¹)		Isotopic Shifts	
	Obs ^a (cm ⁻¹)	Obs ^b (cm ⁻¹)	MP2/ 6-31G ^{*c}	MP2/ 6-31G ^{*a}	Obs ^a (cm ⁻¹)	Obs ^b (cm ⁻¹)	MP2/ 6-31G ^{*c}	MP2/ 6-31G ^{*a}
13-12-13-13-13-12 (M)	1905.2	47.6	47.3	46.4	1912.1 1914.0	47.3 45.0		47.0 44.1
13-12-12-13-13-13 (N)	1905.6	47.2	47.6	46.2	1909.6 1914.0	49.8 45.4		49.3 44.8
13-13-13-12-12-12 (O)	1908.3	44.5	44.5	44.1	1913.2 1920.8	46.2 38.6		45.8 38.9
13-12-12-13-13-12 (P)	1910.7	42.1	42.2	42.9	1917.1 1919.5	42.3 39.9		42.6 40.7
12-13-13-13-12-12 (Q)	1912.7	40.1	40.3	41.5	1916.9	42.5		43.0 37.4
13-12-13-12-13-13 (R)	1912.7	40.1	40.3	39.3	1917.1	42.3		42.5 36.0

^aThis work. Observed values are in Ar matrix at 12K.^bRef (73).^cRef (75).

Table 16. Assignment of C_6H_2O isotopomers (cont.).

Isotopomer	C_6 Molecule			C_6H_2O Molecule		
	Isotopic Shifts		ν (Obs) ^a (cm ⁻¹)	Isotopic Shifts		MP2/ 6-31G** ^a
	Obs ^a (cm ⁻¹)	Obs ^b (cm ⁻¹)		ν (Obs) ^a (cm ⁻¹)	Obs ^a (cm ⁻¹)	
12-13-13-12-12-12 (S)	1914.0	38.8	39.0	38.9	1919.4	39.4 35.0
13-12-13-12-13-12 (I)	1916.9	35.9	36.0	35.7		37.6 33.3
13-13-12-12-12-13 (U)	1917.9	34.7	34.7	34.1		36.8 31.2
13-13-12-13-12-12 (V)	1919.1	33.7	33.8	33.0		37.2 28.2
13-12-12-12-13-12 (W)	1922.9	29.9	29.9	30.0		31.4 28.0
12-13-12-13-12-12 (X)	1923.6	29.2	29.9	29.6		32.7 25.7

^aThis work. Observed values are in Ar matrix at 12K.^bRef (73).^cRef (75).

Table 17. Assignment of $C_6H_5H_2O$ isotopomers (cont.).

Isotopomer	C_6 Molecule				$C_6H_5H_2O$ Molecule		
	Isotopic Shifts		Isotopic Shifts		Isotopic Shifts		MP2/ 6-31G ^a
	ν (Obs) ^a (cm ⁻¹)	Obs ^a (cm ⁻¹)	Obs ^b (cm ⁻¹)	MP2/ 6-31G ^c	ν (Obs) ^a (cm ⁻¹)	Obs ^a (cm ⁻¹)	
13-13-12-12-12-12 (Y)	1925.7	27.1	29.3	28.8			32.4
13-12-13-13-12-13 (Z)	1927.5	25.3	25.9	25.0			24.4
12-13-12-12-12-12 (AA)	1929.5	23.3	23.4	24.9			25.0
13-12-13-13-12-12 (BB)	1931.8	21.0	20.9	20.0			27.4
13-12-13-12-12-13 (CC)	1932.7	20.1	20.2	18.4			21.5
12-12-13-13-12-12 (DD)	1937.1	15.7	15.7	15.1			20.9
							18.5
							18.8
							17.7
							14.7

^aThis work. Observed values are in Ar matrix at 12K.^bRef (73).^cRef (75).

Table 18. Assignment of C_6H_2O isotopomers (cont.).

Isotopomer	C_6 Molecule			C_6H_2O Molecule		
	ν (Obs) ^a (cm ⁻¹)	Isotopic Shifts		ν (Obs) ^a (cm ⁻¹)	Isotopic Shifts	
		Obs ^a (cm ⁻¹)	MP2/ 6-31G* ^c		Obs ^a (cm ⁻¹)	MP2/ 6-31G* ^a
13-12-13-12-12-12 (EE)	1936.7	16.1	16.2	14.6		14.8 13.5
13-12-12-13-12-12 (FF)	1938.9	13.9	14.1	12.6		14.1 10.4
12-12-13-12-12-12 (GG)	1942.8	10.0	10.0	8.8		
13-12-12-12-12-13 (HH)	1943.5	9.3	10.0	9.2		9.1 7.6
13-12-12-12-12-12 (II)	1947.8	5.0	5.0	4.5		9.6
12-12-12-12-12-12 (JJ)	1952.8	(1952.8)	(1952.5)	(1952.5)	1959.4 (1959.4)	5.8 3.5 (1959.4)

^aThis work. Observed values are in Ar matrix at 12K.^bRef (73).^cRef (75).

D. C_3^- Molecule

1. Infrared Absorption Spectra

Several infrared features assigned to $^{12}C_n^-$ species have been observed⁸⁵ and are shown in Figure 40 along with the shifts to the corresponding $^{13}C_n^-$ features. With the exception of the $^{12}C_3^-$ band at 1721.8 cm^{-1} , the remaining bands are tentatively assigned⁸⁵ according to previous work. The electron affinities for C_n molecules are known to lie in the range of 1.995 eV (C_3) to 4.379 eV (C_8)⁹⁰ and the linear even clusters have higher electron affinities than the odd clusters. There are a few features in Figure 40 that should be noted. The band marked at 1643.6 cm^{-1} , whose shape is similar to the $\nu_6(\sigma_u)$ band of linear $^{12}C_8$ at 1710.5 cm^{-1} ¹⁹¹, is tentatively assigned to the $\nu_6(\sigma_u)$ band of linear $^{13}C_8$. The $\nu_7(\sigma_u)$ band of $^{13}C_9$ was previously observed and assigned by Kranze *et al*⁹² and the 1483.8 cm^{-1} is newly observed and assigned to $^{13}C_4$.

Three techniques were used in the identification and assignment of the carbon cluster anions⁸⁵. During annealing of the matrix of neutral clusters, the smaller clusters ($n=3-6$) were observed to decrease in intensity while the reverse was true for the larger clusters. This same behavior was observed for the peaks assigned to carbon cluster anions (C_n^-). Second, the features corresponding to carbon cluster anions decreased in intensity after photolysis of the matrix using a medium pressure Hg lamp. Figure 41 shows the behavior of the C_n^- features as they decreased with photolysis. Finally, the addition of CCl_4 to the Ar matrix gas decreased the intensity of the anions. As mentioned in the previous chapter, CCl_4 and its electron impact products compete as electron acceptors, thereby reducing the concentration of anions in the laser ablated carbon vapor.

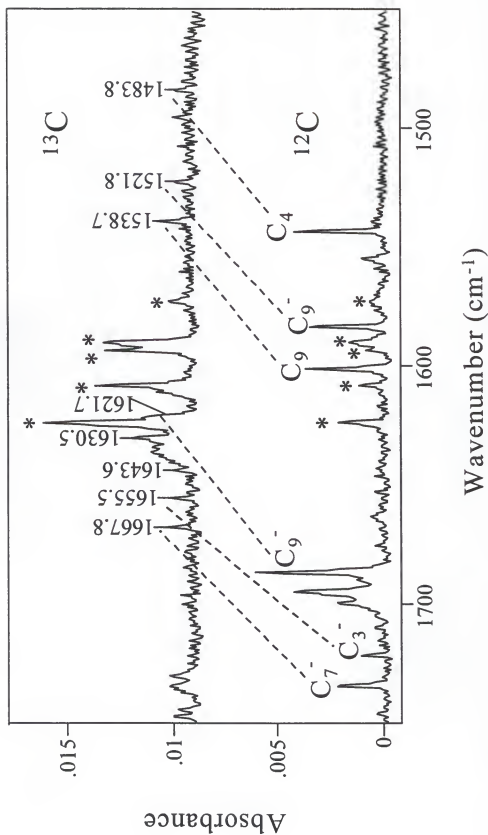


Figure 40. Asymmetric stretch mode region of linear C_n^- ($3 < n < 9$) carbon clusters isolated in an Ar matrix recorded for the ^{13}C isotope (upper spectrum) and the ^{12}C isotope (lower spectrum). H_2O bands are marked by stars (*).

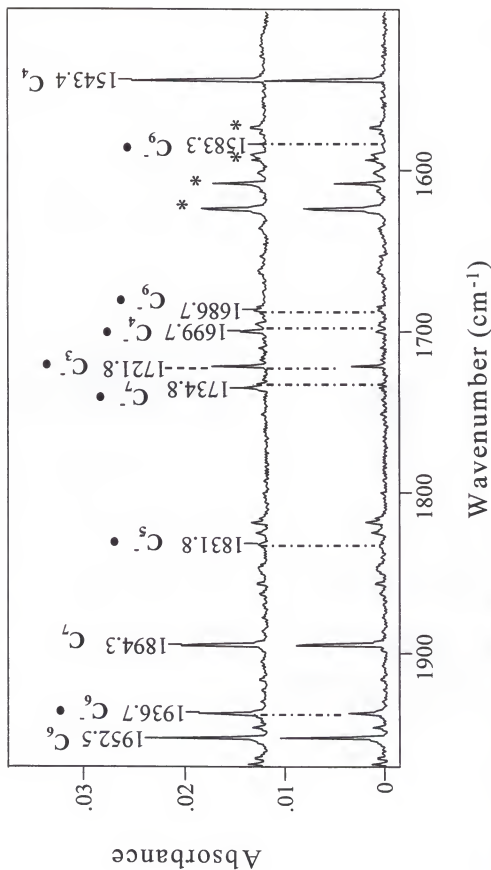


Figure 41. Asymmetric stretch mode of region of linear C_n^- ($3 < n < 9$) carbon clusters isolated in an Ar matrix recorded for the ^{13}C isotope before photolysis (upper spectrum) and after photolysis (lower spectrum). H_2O bands are marked by stars (*).

A similar method was used in the identification of the C_{60} anion band⁹³ where the ratio of C_{60}^-/C_{60}^+ decreased when CCl_4 was added to the matrix gas.

Figures 42 and 43 are the spectra recorded when a 1:1 mixture of $^{12}C/^{13}C$ was laser ablated. The pattern of features in the 1700 cm^{-1} region, shown in Figure 42, which were assigned to the six isotopomers of $^{12/13}C_n^-$, is quite similar to the known $^{12/13}C_3$ neutral spectrum⁹⁴. The spectrum for the neutral isotopomers corresponding to the same run as Figure 42 is shown in Figure 43. In order to reduce the interference from larger C_n clusters observed in Figures 40 and 41, the laser beam photon flux was lowered. Compared to their intensity ratios in those spectra, the tentatively assigned $^{12}C_7^-$ band at 1734.1 cm^{-1} and the C_6 band at 1952.5 cm^{-1} were not discernable in Figures 42 and 43, respectively.

2. Theoretical

The geometry optimizations and harmonic frequencies were carried out using Gaussian 94⁹⁵. Two levels of theory were utilized: (1) the Density Function Theory (DFT) hybrid Becke's three parameter with Lee-Yang-Parr fitting correlation functional (B3LYP) method and (2) the 2nd order correlation Møller-Plesset perturbation theory (MP2) method. The standard 6-31G* and 6-31+G* (diffuse functions added) basis sets were used for each level of theory. A comparison of experimental and theoretical results for various ^{12}C and ^{13}C carbon cluster anions is presented in Table 19. The molecular parameters found at the B3LYP and MP2 levels of theory along with previous coupled cluster [QCISD(T)] results are listed in Table 20. A complete assignment of the six isotopomers of C_3^- along with the comparative theoretical work is shown in Table 21.

$^{12}/^{13}\text{C}_3^-$ in Ar

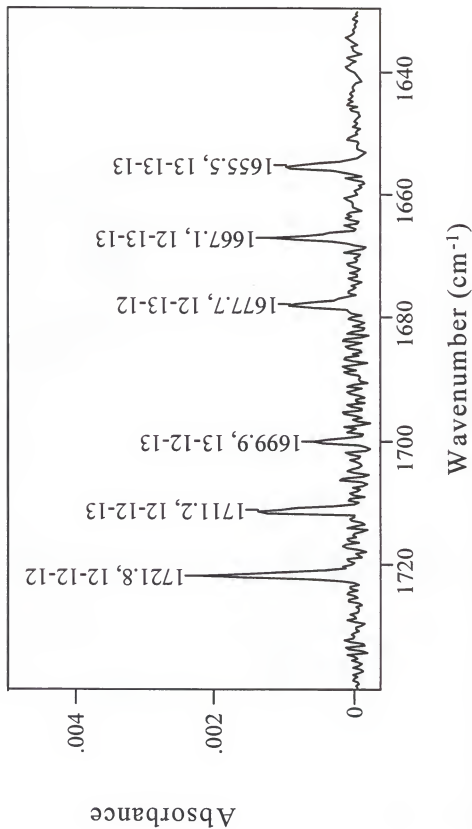


Figure 42. The asymmetric stretch mode absorption spectrum of $^{12}/^{13}\text{C}_3^-$ carbon cluster ions isolated in an Ar matrix at 12K.

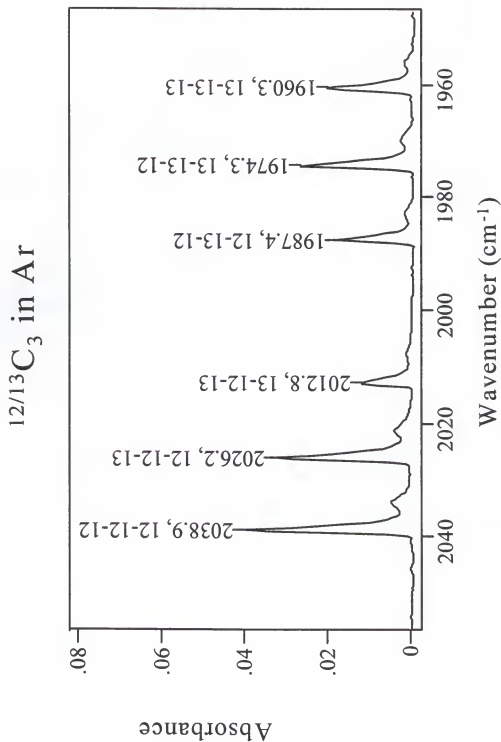


Figure 43. The asymmetric stretch mode absorption spectrum of $^{12}/^{13}\text{C}$ carbon cluster neutral recorded from the same run as Figure 42.

Table 19. IR absorption bands for $^{12}\text{C}_n^-$ and $^{13}\text{C}_n^-$ carbon cluster anions.

Cluster	Mode	Ar matrix			B3LYP/6-31G**		
		ν (cm^{-1}) ^{12}C	ν (cm^{-1}) ^{13}C	$\Delta\nu$ (cm^{-1})	ν (cm^{-1}) ^{12}C	ν (cm^{-1}) ^{13}C	$\Delta\nu$ (cm^{-1})
C_3^-	$\nu_3(\sigma_u)$	1721.8	1655.5	66.3	1721.8	1654.2	67.6
C_5^-	$\nu_3(\sigma_u)^b$	1831.5	1760.9	70.6	1831.5	1759.7	71.8
C_6^-	$\nu_4(\sigma_u)^c$	1936.7	1861.7	75.0	1936.7	1860.5	76.2
C_7^-	$\nu_5(\sigma_u)^b$	1734.8	1667.8	67.0	1734.8	1666.7	68.1
C_9^-	$\nu_6(\sigma_u)^b$ $\nu_6(\sigma_u)^b$	1686.7 1583.3	1621.7 1521.8	65.0 61.5	1686.7 1583.3	1620.6 1521.2	66.1 62.1

^aFrequencies scaled by 0.97189, 0.96268, 0.95095, 0.94503, and 0.92957 and 0.95138 for C_3^- , C_5^- , C_6^- , C_7^- and C_9^- , respectively.^bTentative assignments proposed in Ref[85].^cAssigned based on recent $^{12}/^{13}\text{C}$ isotopic studies⁹⁵.

Table 20. Optimized geometry, harmonic frequencies and rotational constant for electronic ground state C_3^- at different levels of theory.

Geometry:	B3LYP/6-31G*		MP2/6-31G*		QCISD(T)
	6-31G*	6-31+G*	6-31G*	6-31+G*	6-31G** ^a
R (Å)	1.3119	1.3109	1.3068	1.3066	1.322
α (deg)	180.0	180.0	180.0	180.0	180.0
Mode:	ν (cm ⁻¹) [I (km/mol)]	ν (cm ⁻¹) [I (km/mol)]	ν (cm ⁻¹) [I (km/mol)]	ν (cm ⁻¹) [I (km/mol)]	ν (cm ⁻¹)
σ_u	1772.1 [152]	1771.7 [194]	1705.1 [163]	1710.9 [210]	1754
σ_g	1201.9 [0]	1195.8 [0]	1256.6 [0]	1247.5 [0]	1175
π_u	453.4 [28] 319.1 [40]	400.3 [6] 295.3 [28]	470.4 [29] 314.1 [45]	375.1 [7] 246.3 [36]	399 251
Rotational Constant: B (GHz)	12.238791	12.254075	12.3307229	12.334806	

^aRef [87].

Table 21. Vibrational assignments for all $^{12}\text{C}/^{13}\text{C}$ isotopomers of C_3^- carbon cluster ion.

Isotopomer	Theory		Exp	Isotopic Shift	
	B3LYP	MP2 ^b	Ar at 12K	Calc _{B3LYP}	Calc _{MP2}
	6-31G* ^a	6-31+G* ^b	6-31+G* ^c	6-31+G*	6-31+G*
12-12-12	1721.8	1721.8	1721.8	0.0	0.0
12-12-13	1711.1	1711.1	1711.2	10.7	10.6
13-12-13	1699.5	1699.6	1699.9	22.2	22.2
12-13-12	1676.9	1677.1	1677.7	44.7	44.7
12-13-13	1665.9	1666.1	1667.1	55.7	55.6
13-13-13	1654.0	1654.3	1655.5	67.5	67.4
					66.3

^{a, b, c}Frequencies scaled by factors of 0.9176, 0.9178 and 1.0064, respectively

The calculated isotopic shift for the $^{13}\text{C}_3^-$ ($^{13}\text{C}-^{13}\text{C}-^{13}\text{C}$) can be alternatively described by the Teller-Redlich Rule formula,

$$\Delta\nu_{\text{calc}} = \nu_{12\text{C}} \{ 1 - [m(^{12}\text{C})/m(^{13}\text{C})]^{1/2} \} \quad (14).$$

With $\nu_{12\text{C}}$ of the highest energy mode (σ_u) equal to 1721.8 cm^{-1} , $\Delta\nu_{\text{calc}} = 67.76 \text{ cm}^{-1}$. Since this shift was 1.46 cm^{-1} higher in energy than the experimental shift, $\Delta\nu_{\text{exp}} = 66.3 \text{ cm}^{-1}$, a correction factor ($\Delta\nu_{\text{corr}}$) was determined where,

$$\Delta\nu_{\text{corr}} = (1.46 \text{ cm}^{-1} / 67.76 \text{ cm}^{-1}) \Delta\nu_{\text{calc}} = 0.02157 \Delta\nu_{\text{calc}}. \quad (15)$$

The $\Delta\nu_{\text{calc}}$ for the $^{12}\text{C}^{13}\text{C}^{12}\text{C}$ and $^{13}\text{C}^{12}\text{C}^{13}\text{C}$ isotopomers of C_3^- molecule are bond angle dependent and the calculated isotopic shifts for the asymmetric stretch mode [AB_2 type molecule using GF matrix formalism] are

$$\Delta\nu_{\text{calc}} = \nu_{12\text{C}} \{ 1 - [1 - \{(1 - \cos\alpha)(1 - [m(^{12}\text{C})/m(^{13}\text{C})]) / (2 - \cos\alpha)\}]^{1/2} \} \quad (16)$$

and

$$\Delta\nu_{\text{calc}} = \nu_{12\text{C}} \{ 1 - [1 - \{(1 - [m(^{12}\text{C})/m(^{13}\text{C})]) / (2 - \cos\alpha)\}]^{1/2} \}, \quad (17)$$

respectively. Using Equations (16) and (17), and Equation (15), a corrected value for $\Delta\nu_{\text{calc}}$ was calculated where,

$$\Delta\nu_{\text{calc(corr)}} = \Delta\nu_{\text{calc}} - \Delta\nu_{\text{corr}}. \quad (18)$$

The fitting curves for the RMS difference between $\Delta\nu_{\text{calc(corr)}}$ and $\Delta\nu_{\text{exp}}$ versus bond angle (α) for the two AB_2 isotopomers of C_3 and C_3^- are shown in Figure 44. Results for the neutral molecule are shown here to verify the technique on a known geometry. The minimum RMS deviation between the calculated and experimental isotopic shifts for the C_3 molecule occurred at $\alpha = 162^\circ$ which agrees well with the previously determined value of $\alpha = 160.0^\circ$ ⁸⁸. The minimum RMS value (0.15 cm^{-1}) for the C_3^- molecule occurred at $\alpha = 180^\circ$.

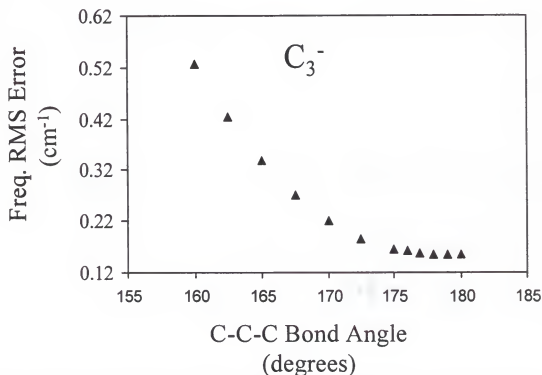
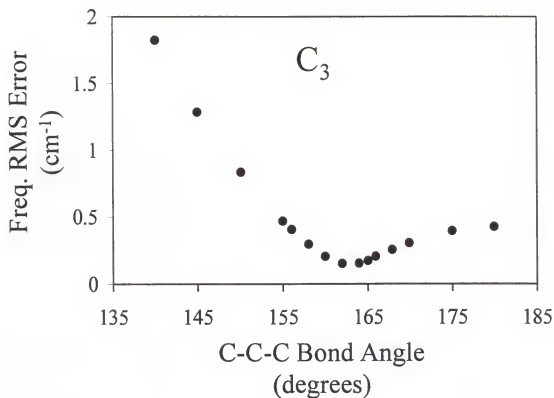


Figure 44. RMS error deviation between calculated and experimental isotopic frequency shifts for the $^{12}C^{13}C^{12}C$ and $^{13}C^{12}C^{13}C$ isotopomers of C_3 and C_3^- versus the C-C-C bond angle, α .

3. Discussion

The optimized geometry for the C_3^- molecule calculated at the B3LYP/6-31G*, B3LYP/6-31+G*, MP2/6-31G* and MP2/6-31+G* levels of theory agree well with calculations at the HF/QCISD(T)/6-31G*, ROHF/DZP and MBPT levels of theory previously reported by Raghavachari⁸⁷, Watts and Bartlett⁹⁶ and Adamowicz⁹⁷, respectively. Adding the diffuse functions to the basis set did not affect the optimized geometry to any degree, however the experimental isotopic shifts were slightly better relative to experimental. In addition, the calculations using the added diffuse functions did result in lowering the frequency of the bending modes.

Comparison of the geometrical parameters of C_3 neutral to the anion provided some interesting observations. The electron configuration of C_3 neutral is $(\sigma_g)^2(\sigma_u)^2(\sigma_g)^2(\sigma_u)^2(\pi_u)^4$ with a $^1\Sigma_g^+$ ground state⁸⁷. The lowest unoccupied orbital, π_g , is the orbital filled by the additional electron in C_3^- . Since the π_g orbital is non-bonding, the bond length for the anionic molecule was expected and observed (See Table 20) to be similar to the neutral C_3 cluster ($R_{C-C}=1.297 \text{ \AA}$).

The second comparison dealt with the rigidity of the anion versus the neutral molecule. Two bending mode frequencies were calculated for the C_3^- molecule at frequencies around 400 and 300 cm^{-1} (See Table 20). The doubly degenerate bending mode frequency for the C_3 neutral molecule was calculated to be 66 cm^{-1} ⁸⁷ and experimentally observed in the gas phase at 63.416529(40) cm^{-1} ⁹⁸. The anionic molecule was expected to be more rigid according to the theoretical bending mode frequencies and the rigidity was verified by Figure 44 where the RMS difference between the experimental and theoretical isotopic shifts was a minimum at $\alpha=180^\circ$. The more floppy

C₃ neutral was perturbed by the Ar matrix to $\alpha=160^\circ$ but the rigidity of the anion precluded the same perturbation.

IV. CONCLUSIONS

A. PAHs

Infrared absorption spectroscopic studies of tetracene and pentacene ions reached the following conclusions:

(1) The most intense features in the infrared spectra of pentacene and tetracene neutral are the out-of-plane CH wagging modes, while the strongest bands for the anion and cation are the in-plane CC stretching modes.

(2) Based on the decrease in intensity of the pentacene anion features upon photolysis, the anions are the least likely candidates as the source of the UIR emission. The anions would probably undergo a very fast photodetachment process in the UV-rich environment of interstellar space.

(3) The band assignments at the B3LYP/4-31G level of theory are in good agreement with cationic and anionic features observed for both tetracene and pentacene. The calculated relative intensities are in reasonable agreement for both neutral molecules except that intensities in the CH stretch region are overestimated.

(4) Based on the intensity ratios of the infrared absorption spectra for tetracene and pentacene, a mixture of neutral and cation PAHs would be needed to account for all the features of UIR emission. However, as was demonstrated in theoretical calculations for neutral PAH molecules, the ratio of band intensities in the emission spectra of a PAH in interstellar space may be quite different than laboratory absorption spectra.

(5) Calculations of theoretical emissions based on infrared spectroscopic data will require the determination of experimental integral intensities. The calculated integral intensities for tetracene neutral and cation were in reasonable agreement with theoretical predictions.

B. $C_n \cdot H_2O$ Complexes

The infrared spectroscopic studies of carbon chain water complexes provided the following conclusions:

(1) The feature at 1959.4 cm^{-1} is assigned to the $C_6 \cdot H_2O$ complex based on the following observations: (a) The ratio of $C_6 \cdot H_2O : C_6$ increases when the concentration of H_2O in the matrix increases. (b) The feature increases in intensity upon annealing the matrix. (c) $^{12,13}C$ isotopic studies are in reasonable agreement with theoretical calculations.

(2) The feature at 2014.4 cm^{-1} is assigned to $C_9 \cdot H_2O$ based on the following observations: (a) The ratio of $C_9 \cdot H_2O : C_9$ increases when the concentration of H_2O in the matrix increases. (b) The theoretical shift (15.5 cm^{-1}) for the water complex versus C_9 is in good agreement with experimental (16.4 cm^{-1}). (c) The bleaching behavior of the $C_9 \cdot H_2O$ feature is similar to that of $C_3 \cdot H_2O$ in that there is a significant decrease in intensity upon photolysis using a glass filter. Both complexes are singlet state molecules, which may account for their similar photolysis behavior.

(3) A feature at 1550.4 cm^{-1} is tentatively assigned to the $C_4 \cdot H_2O$ complex. The band increased in intensity upon annealing the matrix and showed similar photolysis behavior as the $C_6 \cdot H_2O$ complex. Both complexes are triplet state molecules, which may account for their similar photolysis behavior.

C. C_3^- Molecule

Infrared spectroscopic studies on the C_3^- molecule produced the following conclusions:

(1) The calculated isotopic frequency shifts at both the B3LYP and MP2 levels of theory are in very good agreement with the observed experimental isotopomers. Therefore, the band at 1721.8 cm^{-1} can be definitively assigned to the C_3^- molecule.

(2) Isotopic frequency shifts calculated by the GF matrix method were determined for the isotopomers whose frequencies are geometry dependent. By best fitting to experimental values, the geometry of the C_3^- molecule in an Ar matrix was determined to be linear. In contrast, the C_3 molecule in an Ar matrix was determined to have a bent structure with $\alpha=160^\circ$. Calculated frequencies for the bending mode of C_3^- were ~ 400 and $\sim 300\text{ cm}^{-1}$ and predicted that the anion would be more rigid than the neutral molecule.

REFERENCES

- [1] Lewis, G. N.; Lipkin, D.; *J. Amer. Chem. Soc.* **1942**, *64*, 2801.
- [2] Norman, I.; Porter, G.; *Nature* **1954**, *174*, 508.
- [3] Whittle, E.; Dows, D. A.; Pimentel, G. C.; *J. Chem. Phys.* **1954**, *22*, 1943.
- [4] Moskovits, M.; Ozin, G. A.; *Cryochemistry*, ed. M. Moskovits and G. A. Ozin **1976** (New York: John Wiley & Sons).
- [5] Gillet, F. C.; Forrest, W. J.; Merrill, K. M.; *Ap. J.* **1973**, *183*, 87.
- [6] Allamandola, L. J.; Tielens, A. G. G. M.; Barker, J. R.; *Ap. J. Sup.* **1989**, *71*, 733.
- [7] Schutte, W. A.; Tielens, A. G. G. M.; Allamandola, L. J.; *Ap. J.* **1993**, *415*, 397.
- [8] Willner, S. P.; Soifer, B. T.; Russel, R. W.; Joyce, R. R.; Gillett, F. C.; *Ap. J. Lett.* **1977**, *217*, L121.
- [9] Russell, R. W.; Soifer, B. T.; Willner, S. P.; *Ap. J. (Letters)*, **1977**, *217*, L149.
- [10] Allamandola, L. J.; Norman, C. A.; *Astr. Ap.* **1978**, *66*, 129.
- [11] Duley, W. W.; Williams, D. A.; *M. N. R. A. S.* **1981**, *196*, 269.
- [12] Cohen, M.; Allamandola, L. J.; Tielens, A. G. G. M.; Bregman, J.; Simpson, J. P.; Witteborn, F. C.; Wooden, D.; Rank, D.; *Ap. J.* **1986**, *302*, 737.
- [13] Cohen, M.; Tielens, A. G. G. M.; Bregman, J.; Witteborn, F. C.; Rank, D. M.; Allamandola, L. J.; Wooden, D. H.; de Muizon, M.; *Ap. J.* **1989**, *341*, 1989.
- [14] Léger, A.; Puget, J. L.; *Astr. Ap. Lett.* **1984**, *137*, L5.
- [15] Léger, A.; d'Hendecourt, L.; in *Polycyclic Aromatic Hydrocarbons and Astrophysics*, ed. A. Léger, L. d'Hendecourt and N. Boccara, **1987** (Dordrecht: Reidel) 223.
- [16] Allamandola, L. J.; Tielens, A. G. G. M.; Barker, J. R.; *Ap. J. Lett.* **1985**, *290*, L25.

- [17] Birks, J. B.; *Photophysics of Aromatic Molecules*, 1970, (London: Wiley-Interscience).
- [18] Leach, S.; in *Polycyclic Aromatic Hydrocarbons and Astrophysics*, ed. A. Léger, L. d'Hendecourt and N. Boccara, 1987 (Dordrecht: Reidel) 99.
- [19] Clar, E. *The Aromatic Sextet* 1972, (London: Wiley-Interscience).
- [20] Turro, N. J.; *Modern Molecular Photochemistry* 1978, (Menlo Park, CA: Benjamin/Cummings), Chap. 12.
- [21] Van der Zwet, G. P.; Allamandola, L. J.; *Astr. Ap.*, 1985, 146, 76.
- [22] Léger, A.; d'Hendecourt, L.; *Astr. Ap.*, 1985, 146, 81.
- [23] Szczepanski, J.; Vala, M.; Talbi, D.; Parisel, O.; Ellinger, Y.; *J. Chem. Phys.* 1993, 6, 4494.
- [24] Colangeli, L.; Mennela, V.; Baratta, G. A.; Bussolletti, E.; Strazzulla, G.; *Ap. J.* 1992, 396, 369.
- [25] Vodehnal, J.; Stephan, V.; *Collect. Czech. Chem. Commun.* 1971, 36, 3980.
- [26] Cyvin, S.J.; Neerland, G.; Cyvin, B.N.; Brunvoll, J.; *J. Mol. Spec.* 1980, 83, 471.
- [27] Klevens, H. B.; Platt, J. R.; *J. Chem. Phys.* 1949, 17, 470.
- [28] Schmidt, W.; *J. Chem. Phys.* 1977, 66, 828.
- [29] Khan, Z. H.; *Z. Naturforsch* 1984, 39a, 668.
- [30] Shida, T.; *Electronic Absorption Spectra of Radical Cations* 1988, (Amsterdam: Elsevier).
- [31] Andrews, L.; Friedman, R. S.; Kelsall, B. J.; *J. Phys. Chem.* 1985, 89, 4016.
- [32] Kimura, K.; Yamazaki, T.; Katsumata, S.; *J. Phys. Chem.*, 1971, 75, 1768.
- [33] Buschow, K. H. J.; Dieleman, J.; Hoiijtink, G. J.; *J. Chem. Phys.* 1965, 42, 1993.
- [34] Shida, T.; Iwata, S.; *J. Am. Chem. Soc.* 1973, 95, 3473.
- [35] Süzer, S.; Andrews, L.; *J. Chem. Phys.* 1988, 88, 916.

- [36] Szczepanski, J.; Roser, D.; Personette, W.; Eyring, M.; Pellow, R.; Vala, M.; *J. Phys. Chem.* **1992**, *96*, 7876.
- [37] Langhoff, Stephen R.; *J. Phys. Chem.* **1996**, *100*, 2819.
- [38] Khan, Z. H.; Khanna, B. N.; *Can. J. Chem.* **1974**, *52*, 827.
- [39] Frisch, M. J.; Trucks, G. W.; Schlegel, H. B.; Gill, P. M. W.; Johnson, B. G.; Robb, M. A.; Cheeseman, J. R.; Keith, T.; Peterson, G. A.; Montgomery, J. A.; Raghavachari, K.; Al-Laham, M. A.; Zakrzewski, V. G.; Ortiz, J. V.; Foresman, J. B.; Cioslowski, J.; Stefanov, B.; Nanayakkara, A.; Challacombe, M.; Peng, C. Y.; Ayala, P. Y.; Chen, W.; Wong, M. W.; Andres, J. L.; Replogle, E. S.; Gomperts, R.; Martin, R. L.; Fox, D. J.; Binkley, J. S.; Defrees, D. J.; Baker, J.; Stewart, J. P.; Head-Gordon, M.; Gonzalez, C.; Pople, J. A.; *GAUSSIAN 94*, Revision B.2. Gaussian, Inc., Pittsburgh, PA **1995**.
- [40] Cyvin, S.J.; Neerland, G.; Cyvin, B.N.; Brunvoll, J.; *J. Mol. Spec.* **1980**, *83*, 471.
- [41] Szczepanski, J.; Vala, M.; *J. Chem. Phys.* **1993**, *98*, 4494.
- [42] Stüzer, S.; Andrews, L.; *J. Phys. Chem.* **1989**, *93*, 2123.
- [43] Low, G. K. C.; Batley, G. E.; Lidgard, R. O.; Duffield, A. M.; *Biomed. Environ. Mass. Spectrom.* **1986**, *13*, 95.
- [44] Szczepanski, J.; Heldt, J.; *A. Naturforsch.* **1985**, *40*, 849.
- [45] Conley, R. T.; *Infrared Spectroscopy* **1972**, (Boston: Allyn & Bacon).
- [46] Duley, W. W.; Jones, A. P.; *Ap. J. Lett.* **1990**, *351*, L49.
- [47] Szczepanski, J.; Vala, M.; *Ap. J.* **1993**, *414*, 646
- [48] Szczepanski, J.; Vala, M.; *Nature* **1993**, *363*, 699.
- [49] Duley, W. W.; Williams, D. A.; *Interstellar Chemistry* **1984** (London: Academic Press).
- [50] Herzberg, G.; *Ap. J.* **1942**, *96*, 314.
- [51] Swints, P.; *Rev. Mod. Phys.* **1942**, *14*, 190.
- [52] McKellar, A.; *Ap. J.* **1948**, *108*, 453.
- [53] Douglas, A. E.; *Ap. J.* **1951**, *114*, 466.

- [54] Tsuji, T.; *Ann. Tokyo Astr. Obs.* **1964**, 9, 1.
- [55] Turner, B. E.; *Ap. J. Lett.* **1971**, 163, L35.
- [56] Avery, L. W.; Broten, N. W.; MacCleod, J. M.; Oka, T.; Kroto, H. W.; *Ap. J. Lett.* **1976**, 205, L173.
- [57] Kroto, H. W.; Kirby, C.; Walton, D. R. M.; Avery, L. W.; Groten, N. W.; MacCleod, J. M.; Oka, T.; *Ap. J. Lett.* **1978**, 219, L133.
- [58] Broten, N. W.; Oka, T.; Avery, L. W.; MacLeod, J. M.; Kroto, H. W.; *Ap. J. Lett.* **1976**, 223, L105.
- [59] Bell, M. B.; Feldman, P. A.; Kwok, S.; Matthews, H. E.; *Nature* **1982**, 295, 389.
- [60] Kroto, H. W.; Heath, J. R.; O'Brien, S. C.; Curl, R. F.; Smalley, R. E.; *Nature* **1985**, 318, 162.
- [61] Kroto, H. W.; Heath, J. R.; O'Brien, S. C.; Curl, R. F.; Smalley, R. E.; *Ap. J.* **1987**, 314, 352.
- [62] Hinkle, K. H.; Keady, J. J.; Bernath, P. F.; *Science* **1988**, 241, 1319.
- [63] Bernath, P. F.; Hinkle, K. H.; Keady, J. J.; *Science* **1989**, 244, 562.
- [64] Douglas, A. E.; *Nature* **1979**, 269, 130.
- [65] Chupka, W. A.; Inghram, M. G.; *J. Chem. Phys.* **1954**, 22, 1472.
- [66] Honig, R. E.; *J. Chem Phys.* **1954**, 22, 126.
- [67] Pitzer, K. S.; Clementi, E.; *J. Am. Chem. Soc.* **1959**, 81, 4477.
- [68] Weltner, Jr., W.; Van Zee, R. J.; *Chem. Rev.* **1989**, 89, 1713.
- [69] Weltner, W., Jr.; McLeod, D., Jr.; *J. Chem. Phys.* **1964**, 40, 1305.
- [70] Vala, M.; Chandrasekhar, T. M.; Szczepanski, J.; Van Zee, R. J.; Weltner, W., Jr.; *J. Chem. Phys.* **1989**, 90, 595.
- [71] Shen, L. N.; Graham, W. R. M.; *J. Chem. Phys.* **1989**, 91, 5115.
- [72] Heath, J.R.; Saykally, R.J.; *J. Chem. Phys.* **1991**, 94, 3271.

- [73] Vala, M.; Chandrasekhar, T. M.; Szczepanski, J.; Pellow, R.; *High Temperature Science* **1990**, 27, 19.
- [74] Martin, J. M. L.; François, J. P.; Gijbels, R.; *J. Chem. Phys.* **1990**, 93, 8850.
- [75] Kranze, R. H.; Graham, W. R. M.; *J. Chem. Phys.* **1993**, 98, 71.
- [76] Kranze, R. H.; Rittby, C. M. L.; Graham, W. R. M.; *J. Chem. Phys.* **1996**, 105, 5313.
- [77] Kranze, R. H.; Withey, P. A.; Rittby, C. M. L.; Graham, W. R. M.; *J. Chem. Phys.* **1995**, 103, 6841.
- [78] Ahmed, S. N.; McKee, M. L.; Shevlin, P. B.; *J. Am. Chem. Soc.* **1983**, 105, 3942.
- [79] Ortman, B. J.; Hauge, R. H.; Margrave, J. L.; Kafafi, Z. H.; *J. Phys. Chem.* **1990**, 94, 7973.
- [80] Irvine, W. M.; Brown, R. D.; Cragg, D. M.; Friberg, P.; Godfrey, P. D.; Kaifu, N.; Matthews, H. E.; Ohishi, M.; Suzuki, H.; Takeo, H.; *Ap. J. Lett.* **1989**, 335, L89.
- [81] Liu, R.; Zhou, X.; Pulay, P.; *J. Phys. Chem.* **1992**, 96, 5748.
- [82] Szczepanski, J.; Ekern, S.; Vala, M.; *J. Phys. Chem.* **1995**, 99, 8002.
- [83] Szczepanski, J.; Ekern, S.; Chapo, C.; Vala, M.; *J. Chem. Phys.* **1996**, 211, 359.
- [84] Freivogel, P.; Fulara, J.; Jakobi, M.; Forney, D.; Maier, J. P.; *J. Chem. Phys.* **1995**, 103, 54.
- [85] Szczepanski, J.; Ekern, S.; Vala, M.; *J. Phys. Chem. A* **1997**, 101, 1841.
- [86] Forney, D.; Fulara, J.; Freivogel, P.; Jakobi, M.; Lessen, D.; *J. Chem. Phys.* **1995**, 103, 48.
- [87] Raghavachari, K.; *Chem. Phys. Letters* **1990**, 171, 249.
- [88] Szczepanski, J.; Vala, M.; *J. Chem. Phys.* **1993**, 10, 7371.
- [89] Martin, J. M. L.; Taylor, P. R.; *J. Phys. Chem.* **1996**, 100, 6047.
- [90] Arnold, D. W.; Bradforth, S. E.; Kitsopoulos, T. N.; Neumark, D. M.; *J. Chem. Phys.* **1991**, 95, 8753.
- [91] Szczepanski, J.; Ekern, S.; Chapo, C.; Vala, M.; *J. Chem. Phys.* **1996**, 210, 359.

- [92] Kranze, R. H.; Withey, P. A.; Rittby, C. M. L.; Graham, W. R. M.; *J. Chem. Phys.* **1995**, *103*, 6841.
- [93] Gasyna, Z.; Andrews, L.; Schatz, P. N.; *J. Phys. Chem.* **1992**, *96*, 1525.
- [94] Weltner Jr. W.; *Science* **1967**, *155*, 155.
- [95] Szczepanski, J.; Wehlburg, C.; Auerbach, E.; Vala, M.; manuscript in preparation.
- [96] Watts, J. D.; Bartlett, R. J.; *J. Chem. Phys.* **1992**, *97*, 3445.
- [97] Adamowicz, L.; *Chem. Phys. Letters* **1991**, *182*, 45.
- [98] Schmittenmaer, C. A.; Cohen, R. C.; Pugliano N.; Heath, J. R.; Cooksey, A. L.; Basarow, K. L.; Saykally, R. J.; *Science* **1990**, *249*, 897.

BIOGRAPHICAL SKETCH

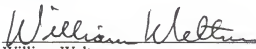
Christine Marie Wehlburg, previously Christine Marie Polesnak, born December 29, 1964, in Worcester, Massachusetts, is the daughter of Stephen and Marie Polesnak. She earned her Bachelor of Science in chemistry from the University of Florida in December 1991. Christine remained at the University of Florida for her graduate studies and earned a Doctor of Philosophy in chemistry in August 1997. As a graduate student, Christine Wehlburg was a NASA Space Grant Fellow for three years from 1994 to 1997. She married Joseph C. Wehlburg in November 1993 and continued to expand her family with the birth of a daughter, Rachel, in December 1994. She and her husband plan to continue their professional careers with post-doctoral positions at Sandia National Laboratories in Albuquerque, New Mexico.

I certify that I have read this study and that in my opinion it conforms to acceptable standards of scholarly presentation and is fully adequate, in scope and quality, as a dissertation for the degree of Doctor of Philosophy.



Martin Vala
Professor of Chemistry

I certify that I have read this study and that in my opinion it conforms to acceptable standards of scholarly presentation and is fully adequate, in scope and quality, as a dissertation for the degree of Doctor of Philosophy.



William Weltner
Professor of Chemistry

I certify that I have read this study and that in my opinion it conforms to acceptable standards of scholarly presentation and is fully adequate, in scope and quality, as a dissertation for the degree of Doctor of Philosophy.



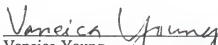
N. Yngve Olsen
Professor of Chemistry

I certify that I have read this study and that in my opinion it conforms to acceptable standards of scholarly presentation and is fully adequate, in scope and quality, as a dissertation for the degree of Doctor of Philosophy.



Alan Jacobs
Professor of Nuclear and Radiological
Engineering

I certify that I have read this study and that in my opinion it conforms to acceptable standards of scholarly presentation and is fully adequate, in scope and quality, as a dissertation for the degree of Doctor of Philosophy.



Vaneica Young
Associate Professor of Chemistry

This dissertation was submitted to the Graduate Faculty of the Department of Chemistry in the College of Liberal Arts and Sciences and to the Graduate School and was accepted as partial fulfillment of the requirements for the degree of Doctor of Philosophy.

August 1997

Dean, Graduate School